Testing of a Hinged Wing-Tip Device for Gust Loads Alleviation

Ronald C. M. Cheung[*], Djamel Rezgui[†] and Jonathan E. Cooper[‡]
University of Bristol, University Walk, Bristol, BS8 1TR, UK.

and
Thomas Wilson[§]
Airbus Operations Ltd, Filton, Bristol, BS34 7PA, UK.

Recent aircraft designs have considered higher aspect ratio wings to reduce induced drag for improved fuel efficiency; however, to remain compliant with airport gate requirements, folding wing-tips have been introduced as a solution to the increased wing-span. Recent numerical studies suggest that a folding wing-tip solution may be incorporated with spring devices to provide an additional gust loads alleviation ability in flight as well. In this work, a series of low-speed steady and dynamic wind tunnel tests was conducted using a prototype of such a concept. It was found that a folding wing-tip with a non-zero relative angle of the folding hinge axis to the stream-wise direction could provide gust loads alleviation. The level of load alleviation varied with hinge spring stiffness and lifting condition, with the best performance achieving a 56% reduction in peak loading.

Nomenclature

α = *Angle of attack*

γ = *Hinge angle*

Λ = *Sweep angle*

θ = *Fold angle of the wing-tip*

k_θ = *Torsional spring stiffness*

k_x = *Linear spring stiffness*

V = *Velocity*

x = *Linear displacement*

[*] Research Associate, Department of Aerospace Engineering.
[†] Lecturer in Aerospace Engineering, Department of Aerospace Engineering.
[‡] Airbus Royal Academy of Engineering Sir George White Professor of Aerospace Engineering, Department of Aerospace Engineering. Associate Fellow AIAA.
[§] Head of Technical Capability for Aircraft Loads, Flight Physics Department.

I. Introduction

The classic Breguet range equation shows that aircraft with more fuel-efficient engines, lower aerodynamic drag or lower structural weight can fly further. Therefore, an aircraft with any of these attributes can cover the same distance either carrying a larger payload or using less fuel. For airframe design, these criteria lead to targeting the aerodynamics and structural weight for improved performance. One approach for improving the aerodynamics is to increase the aspect ratio of the wing, which decreases the associated induced drag. However, increasing the wing span not only increases structural weight, it could also lead to operating difficulties as existing airport gates may be too narrow and operating cost could increase as airlines are charged according to the size of the gates that their aircraft use. Trying to enable these conflicting planform requirements points towards the wider field of morphing structures, which in some approaches focus on changing the geometry of the aircraft during operation. The field of morphing covers larger planform geometric changes including sweep and span [1, 2] to finer shape changes such as camber, which tend to be more focused on application of specific materials [3-6] or fabricated products [7].

One of the simplest morphing solutions for variable span requirement is in the form of a folding wing-tip, which is already deployed in the latest Boeing 777 airline [8], as it can be achieved using conventional materials through a hinged design. The hinge mechanism allows the wing-tip to be either folded up as the aircraft taxis to the gate or locked in its extended position before takeoff and during flight. Morphing of aircraft wing-tips has received significant interest as there is a great potential to enabling optimized aerodynamic performance for varying conditions throughout each flight.

Flexible wing-tips have also been suggested to enable passive gust loads alleviation as the large moment arm offered by a wing-tip device has a greater influence upon the bending moment distribution along the wing. Several studies [9-13] have employed a passive movable aerodynamic surface at the wing-tip with the device being connected to the main airframe through a torque tube in the span-wise direction about a location forward of the wing-tip's center of pressure. The device functioned by reacting to vertical gusts through a resulting nose-down deflection in a passive manner, alleviating the load increment caused by the gusts. Although good loads alleviation capability was observed, it had a detrimental effect on flutter, especially when low torsional stiffness torque tubes were used.

Another approach for gust loads alleviation is through a folding wing-tip device that has its hinge axis offset from the longitudinal axis of the aircraft [14]. As the wing-tip folds upwards, the angle that the wing-tip makes relative to the oncoming flow, or its angle of attack, changes by

$$\Delta\alpha = -\tan^{-1}(\tan\theta \sin\gamma) \tag{1}$$

where hinge angle γ describes the angle between the hinge axis and the flow direction $\boldsymbol{V}$ in the global x-y plane, while fold angle θ is the angular displacement of the wing-tip about the hinge axis from the wing-level position as illustrated in Fig. 1.

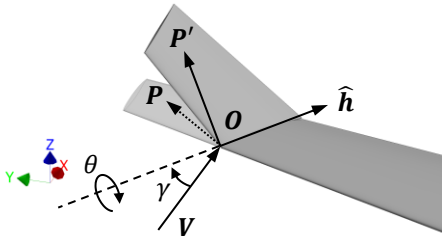

Fig. 1 Definition of hinge angle γ and fold angle θ.

Equation (1) can be derived by first considering the junction between the leading edge and folding hinge line as the origin of the global frame, $\boldsymbol{O}$, and a point $\boldsymbol{P}$ on the wing-tip. The position of $\boldsymbol{P}$ upon folding of the wing-tip is found through Rodrigues' rotation formula [15]

$$\boldsymbol{P}' = \boldsymbol{P}\cos\theta + \left(\hat{\boldsymbol{h}} \times \boldsymbol{P}\right)\sin\theta + \hat{\boldsymbol{h}}\left(\hat{\boldsymbol{h}} \cdot \boldsymbol{P}\right)(1 - \cos\theta) \tag{2}$$

where $\hat{\boldsymbol{h}}$ is a unit vector in the hinge axis direction:

$$\hat{\boldsymbol{h}} = \begin{Bmatrix} \cos\gamma \\ -\sin\gamma \\ 0 \end{Bmatrix} \tag{3}$$

The unit normal of the wing-tip is given by

$$\hat{\boldsymbol{n}}' = \frac{\hat{\boldsymbol{h}} \times \boldsymbol{P}'}{\left|\hat{\boldsymbol{h}} \times \boldsymbol{P}'\right|} = \begin{Bmatrix} -\sin\theta\sin\gamma \\ -\sin\theta\cos\gamma \\ \cos\theta \end{Bmatrix} \tag{4}$$

The change in angle of attack of the wing-tip due to folding is then the angular difference between this normal vector and the global z axis, about the global y axis. Therefore,

$$\tan\Delta\alpha = \frac{\hat{n}'_1}{\hat{n}'_3} = \frac{-\sin\theta\sin\gamma}{\cos\theta} \tag{5}$$

Equation (5) is then rearranged to give Equation (1).

As shown in Fig. 2(a), a zero-value hinge angle produces no change in the angle of attack of the wing-tip, whereas a positive hinge angle, as shown in Fig. 2(b), could provide potential loads alleviation benefit during

vertical gust encounters due to the decreased angle of attack beyond the fold thereby reducing the resulting bending moment contribution along the wing.

(a) Hinge angle of 0^0, $\Delta\alpha = 0$ (b) Hinge angle of 30^0, $\Delta\alpha < 0$

Fig. 2 Front view showing wing-tip at a positive fold angle.

Therefore, a folding wing-tip incorporating a non-zero hinge angle has the potential to both fulfill the airport gate requirement and provide gust loads alleviation capability. A preliminary numerical study [14] was carried out to investigate the feasibility and performance of using a device of this type, with the addition of a passive spring system at the hinge to control its dynamic behavior and exploit its potential gust loads alleviation capability. Along with a further study [16], they have both found that a linear spring device can provide load-alleviating benefit when the hinge stiffness and the wing-tip inertia are low. However, low hinge stiffness can cause the wing-tip to remain in a deflected position even in a trimmed-flight condition, which has an undesirable effect on the overall aerodynamics. This differing optimal stiffness for trimmed-flight and gust loads alleviation has led to proposed solutions such as bi-stable wing-tips [17] and active control via piezoelectric actuators [18]. Despite this complication, the folding wing-tip concept remains promising as recent research have suggested that coupling the folding wing-tip to a nonlinear spring system may provide the solution [19, 20].

This paper describes the first experimental study carried out on a folding wing-tip concept of this kind for gust loads alleviation. Through low-speed wind tunnel testing, the study aimed to obtain baseline experimental data of the folding wing-tip concept configured with a non-zero hinge angle and evaluate its gust loads alleviation performance when it is additionally coupled with a linear spring device.

II. Wind Tunnel Model

A. Folding wing-tip model design

The primary aim of this investigation was to establish the overall gust loads alleviation performance of a folding wing-tip with a non-zero hinge angle. Since the main measure of gust loads alleviation is the reduction in peak wing-root bending moment, the wind tunnel model design was maximized to the largest permissible semi-span for the wind tunnel working section at 0.7m with a constant un-swept chord of 0.3m, using a symmetric NACA0015 section profile as shown in Fig. 3.

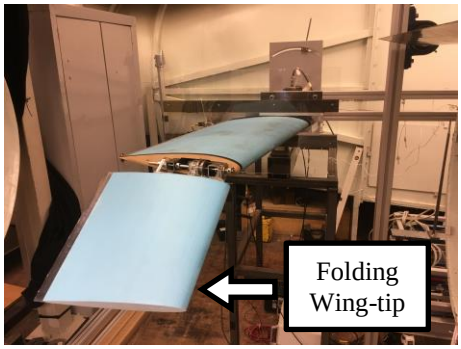

Fig. 3 Wind tunnel model of the folding wing-tip concept.

The choice of a comparatively thick NACA0015 section profile was based on the need to increase the internal volume for fitting a spring system to the folding hinge, which uses a cable linkage to connect the hinge mechanism to springs located outside the wind tunnel.

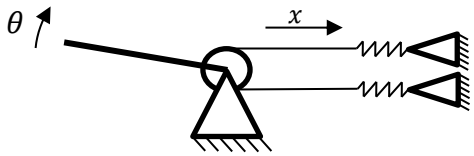

Fig. 4 Schematic of the spring system used in the folding wing-tip wind tunnel model.

The cable linkage functions by translating the angular displacement of the wing-tip, θ, into translational displacement of the cable, x, as shown in Fig. 4. This arrangement allows the use of linear tension springs to represent a torsion spring fitted at the hinge, in which the equivalent torsional stiffness can be derived from the expression for the spring torque about the hinge:

$$T = k_\theta \Delta\theta = k_x \frac{dx}{d\theta} \Delta x \tag{6}$$

As shown in Fig. 5(a), a pulley with a constant groove depth was installed at the hinge. The purpose of this pulley was to ensure the cables were always pulling at the same tangential direction and radial distance from the hinge axis, as illustrated by Fig. 5(b) and (c). Implementing such an approach caused the derivative in Equation (6) to become invariant, so that the same effective torsional stiffness could be maintained within the working range of wing-tip fold angle. The dual-cable design also enables both cables to remain in tension at all fold angles through pre-tensioning, thus ensuring consistency in the spring tension provided by both springs.

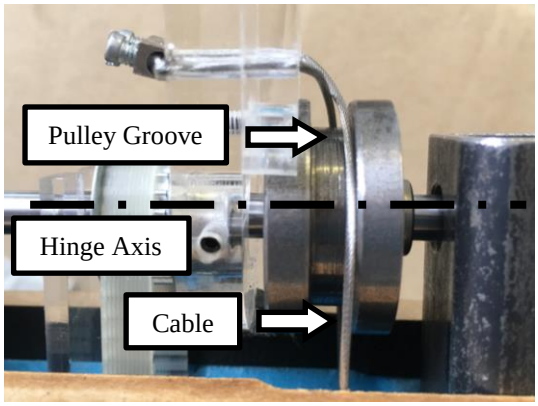

(a) Pulley and cable mechanism.

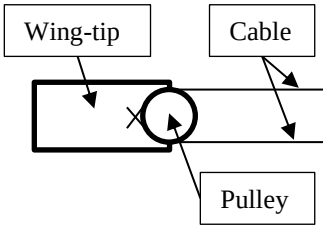

(b) Low fold angle

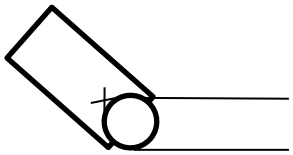

(c) High fold angle

Fig. 5 Cable fixture at the folding hinge.

With future testing in mind, a decision was made to incorporate variable sweep up to 30 degrees into the wind tunnel model, while keeping the hinge axis fixed relative to the body of the model itself. This approach allows the effective hinge angle to be varied through changing the sweep angle of the wing. The orientation of the hinge axis is normal to the leading edge, thus giving a simply mapping between the hinge angle and the sweep angle as the following:

$$\gamma = \Lambda \tag{7}$$

As illustrated in Fig. 6, the variable sweep design involves shielding the wing-root from the airflow, therefore as the sweep angle is increased, the total exposed wing area and wing span are reduced. To compensate for these changes, a customized wing-tip sized to 33% of the total exposed wing area was used at each test sweep angle. Foam construction was used to ease the manufacturing process, as well as minimizing mass and inertia of the wing-tips.

(a) Low sweep angle (10 degrees) (b) High sweep angle (30 degrees)

Fig. 6 Variable sweep design configuration.

Given the possible variation in sweep configuration, there was also a need to suppress the inherent bend-twist coupling in all swept wing configurations, such that the effect of the folding wing-tip could be better isolated. This requirement was fulfilled by incorporating a full-length 25x25x2mm mild steel box section as the front spar and a 20x20x2mm section as the rear spar into the non-folding part of the wind tunnel model, as bench testing showed an averaged vertical displacement of less than 3mm along the hinge line and an in-plane rotation of less than 2 degrees, when a 49N downwards load was applied to the rear spar at the hinge. Since the resultant wing bending and torsion load in this bench test was higher than those expected in the most severe wind tunnel test condition, these displacements were deemed sufficiently small and thus no measurements were taken during the wind tunnel testing phase.

B. Test set-up and instrumentation

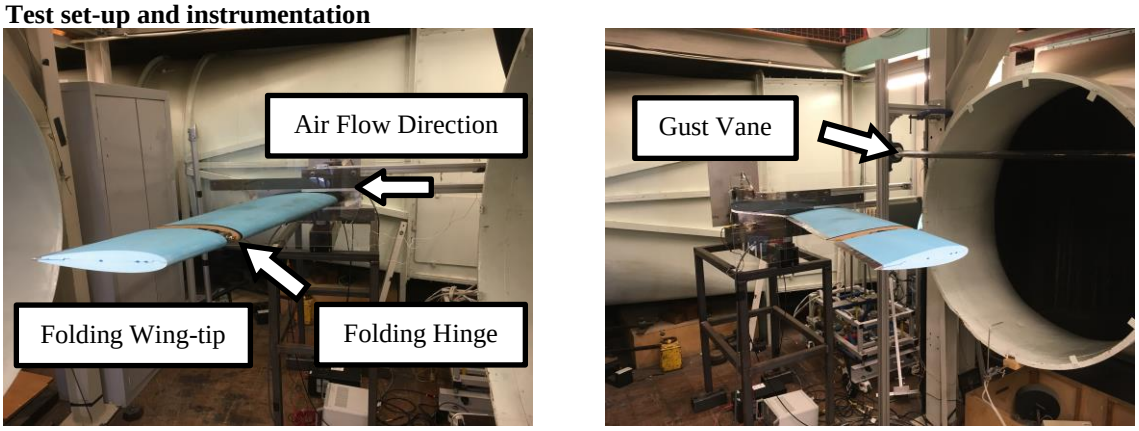

(a) Steady-state. (b) Gust excitation.

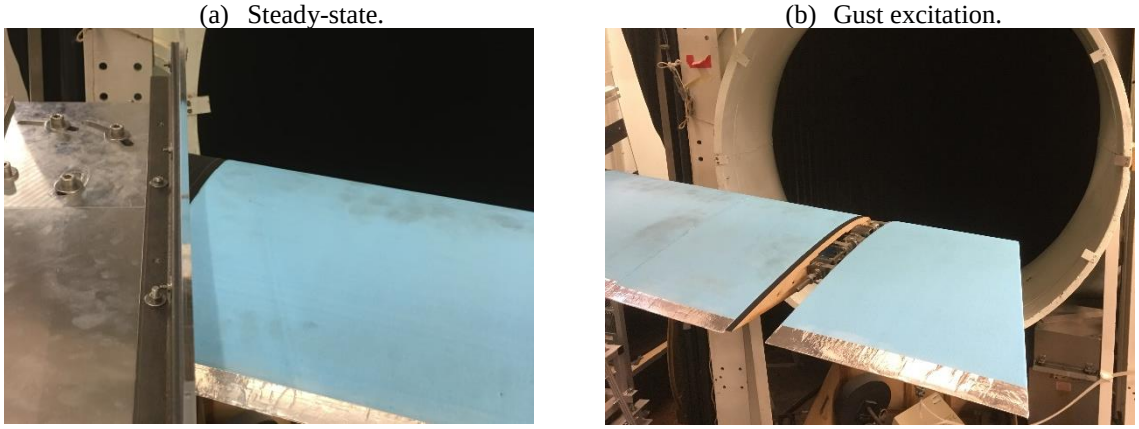

(c) Wing-root location. (d) Wing-tip location.

Fig. 7 Wind tunnel set-up.

The wind tunnel tests were carried out in the open-jet wind tunnel at the University of Bristol, as shown in Fig. 7. The wind tunnel is of a closed-circuit design with a contraction nozzle exit diameter of 1.1m. At speed of 20m/s, the turbulence level at the centerline of the nozzle exit was 1.4%. The test campaign examined the behavior of the wind tunnel model in steady-state conditions as well as its response to gust excitation. In each test, lift, rolling moment and fold angle were measured using the sensors listed in Table 1. Signals from these sensors were captured using a National Instruments USB-6211 interface through LabVIEW software [21]. The reference axis for the rolling moment measurement was parallel to the wing root, therefore such measurement was a key performance metric in the gust excitation cases, as it could be related directly to the magnitude of root bending moment the wing experienced.

Table 1. Sensors used for data acquisition.

Measurement	Sensor	Precision
Lift	AMTI MC3A-250 & AMTI MC3A-1000 [22]	±0.2N
Rolling moment	AMTI MC3A-250 & AMTI MC3A-1000	±0.09Nm
Fold angle	RLS RE22 [23]	±0.1deg

The wind tunnel model was configured for sweep angle of 10 degrees and 30 degrees during this test campaign, corresponding to hinge angle of 10 degrees and 30 degrees respectively. For clarity and convenience, each configuration will be referred to the name given in Table 2 from here onwards.

Table 2. Reference dimensions of the wind tunnel model configurations.

Configuration	Sweep/hinge angle, deg	Reference chord, m	Reference semi-span, m
SWP10	10	0.305	0.856
SWP30	30	0.346	0.711

In addition to the planform variation, three folding hinge arrangements were also examined: stiff-hinge, sprung-hinge and free-hinge. The sprung-hinge arrangement was set up using two linear springs, each with measured stiffness of k_x=195N/m, in the manner illustrated in Fig. 5. This set-up gave an equivalent torsional stiffness of k_0=0.042Nm/rad since the groove radius of the pulley was 10.5mm. Pre-loading of the springs was applied to trim the net hinge moment to zero at fold angle of zero. The stiff-hinge arrangement was achieved by removing the springs and fixing the cables directly, while the free-hinge arrangement was set up simply through disconnecting the cables from the wing-tip.

Table 3. Test matrix for steady-state measurements.

Parameter	Value
Model configuration	SWP10, SWP30
Hinge arrangement	stiff-hinge, free-hinge
Angle of attack, deg	-10,-5,0,5,10
Wind tunnel velocity, m/s	10,12,15,18,20

The test matrix for the steady-state and the gust excitation cases are summarized in Table 3 and Table 4 respectively. The gust excitation cases required installation of a single-vane gust generator, as pictured in Fig. 7(b), ahead of the wind tunnel model to perturb the oncoming flow. At each test point, the gust vane was actuated manually in the upwards direction to a peak displacement of 10.0 degrees and back to its neutral position over a period of 0.4s. Mechanical stops were incorporated to the gust generator mechanism to ensure consistency in the gusts generated and each test was also repeated three times to improve the confidence level in the results collected.

Table 4. Test matrix for gust excitation measurements.

Parameter	Value
Model configuration	SWP10, SWP30
Hinge arrangement	stiff-hinge, sprung-hinge, free-hinge
Angle of attack, deg	-10,-5,0,5,10
Wind tunnel velocity, m/s	20

III. Numerical modeling

In order to allow future exploration of the design space in a more time-efficient manner, numerical Finite Element Models (FEM) were first created in NASTRAN. Aeroelastic predictions were then calculated via the Doublet Lattice Method (DLM) [24, 25] within NASTRAN. To reflect the two sweep configurations of the wind tunnel model, a separate aeroelastic FEM was built for each configuration, as shown in Fig. 8. As explained in the previous section, the exposed area of the wind tunnel model changes with the variable sweep design, therefore the reference dimensions of each configuration were adjusted according to Table 2.

A. Structural Modeling

Each FEM was built using 15726 elements, of which 164 were two-dimensional bar elements, 240 three-

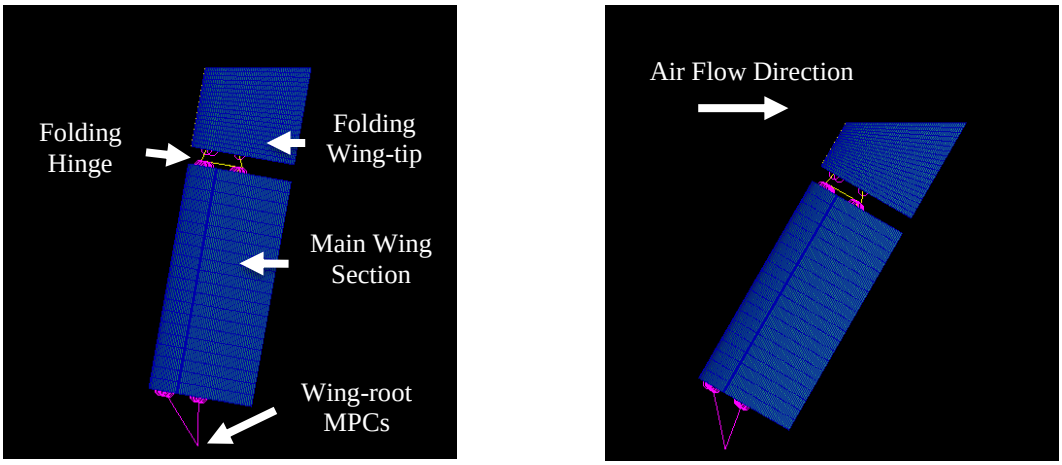

(a) SWP10. (b) SWP30.

Fig. 8 Finite element models (see Table 2 for their properties).

dimensional wedges and 15120 three-dimensional hexahedral elements, as well as a zero-dimensional point-mass. This level of discretization was sufficient since mesh convergence was demonstrated in the first few modal frequencies, as shown in Fig. 9. The three-dimensional elements in each FEM were used to model the exterior of the wing, while the front and rear spars of the main body of the wing and the stiffeners inside the wing-tip were modelled by the bar elements. PBARL cards are used with these bar elements to model the standard beam sections they represent in the physical wind tunnel model.

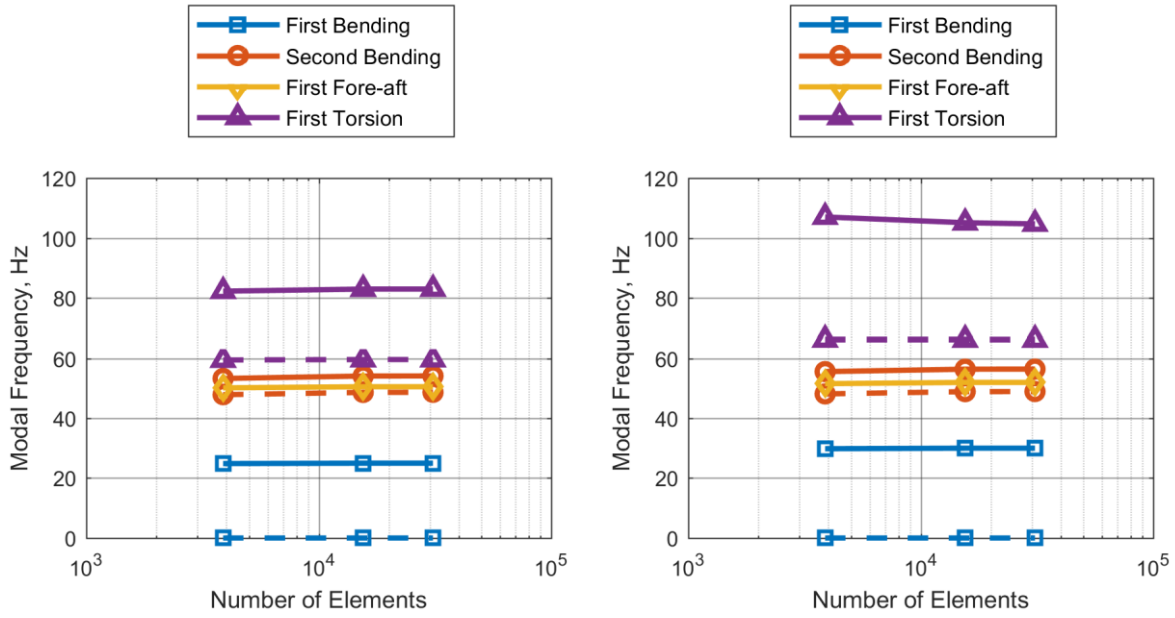

(a) SWP10 (b) SWP30

Fig. 9 FEM mesh convergence (solid line: k_θ=1E9Nm/rad; broken line: k_θ=1E-6Nm/rad).

Multi-point constraints (MPCs) were used for connecting the bar elements to the three-dimensional elements without additional stiffness occurring in the structural representation. As shown in Fig. 8(a), each FEM was also constrained using a single MPC to the root end of the two spar members, and then held to a single point using a fully constrained boundary condition. This set-up allows all reaction loads to be computed at a single point therefore easing the post-processing necessary for comparing against wind tunnel balance measurements, as this single point constraint coincides with the location in space where the wind tunnel balance loads calibration was carried out.

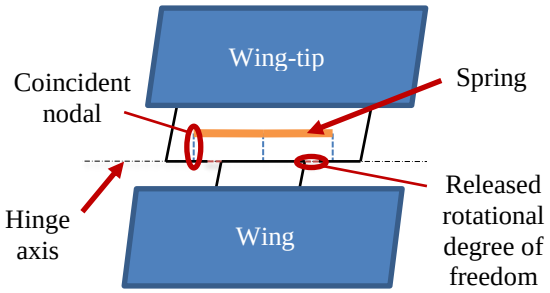

Fig. 10 Schematic of the hinge arrangement in the FEM. (Hinge springs are offset from the hinge axis for clarity.)

As shown in Fig. 10, the hinge of the folding wing-tip was modelled by releasing the rotational degree of freedom in the bar elements that represents the hinge shaft. The hinge stiffness, k_θ, was then specified using two CBUSH spring elements. These CBUSH elements are general six-degrees-of-freedom springs that allow specification of each individual directional stiffness. Thus, it was only necessary to specify the aligned torsional

stiffness to fully represent the effective torsional stiffness about the hinge. Since these two CBUSH elements were operating in parallel, the total hinge stiffness was therefore the sum of their spring rates. To simulate a stiff-hinge configuration, the stiffness of each CBUSH element was set to a very high value and vice versa for the free-hinge configuration. Finally, a point-mass was included in the wing-tip of the FEM as a supplementary mass to match the total mass and center of mass position of the wing-tip of the wind tunnel model.

B. Aerodynamics Modeling

NASTRAN provides aerodynamic loads prediction capability through the Doublet Lattice Method (DLM). DLM is a linear method based on the linearized potential flow theory, which is applicable to low speed, small angle of attack flows. However, this assumption also means that flow features such as flow separation are not represented. Therefore, some discrepancy between the aerodynamic prediction and wind tunnel measurement is expected, especially when the exposed hinge is featured in the wind tunnel model which could adversely affect the flow nearby.

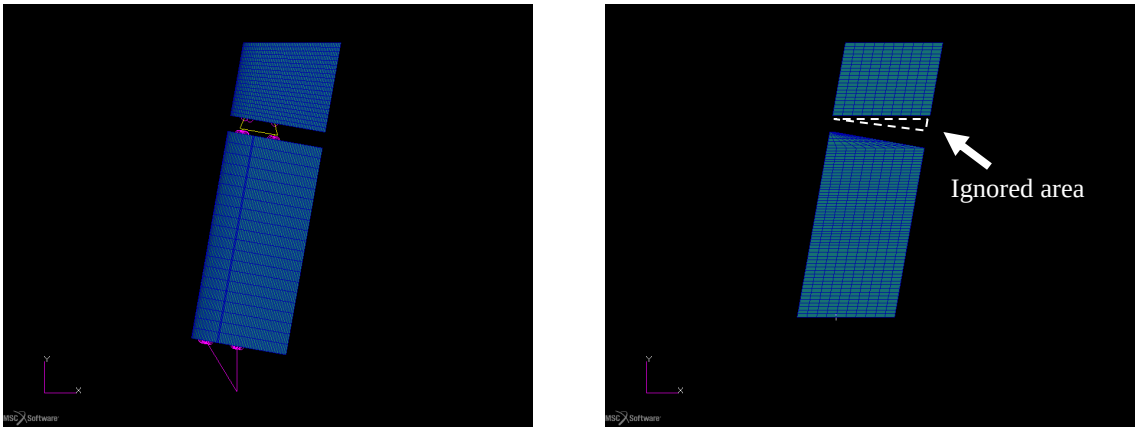

(a) Structural FEM. (b) Aerodynamic panels.

Fig. 11 Aeroelastic FEM of the SWP10 configuration.

A total of 800 aerodynamic panels were used in each aeroelastic FEM and their typical arrangement is shown in Fig. 11. This level of discretization was driven by a mesh convergence study focusing on the peak gust load prediction. As illustrated in Fig. 12, the solution was well within the asymptotic range. As shown in Fig. 11(b), a triangular region around the inboard area of the wing-tip was deliberately ignored due to geometric limitation of DLM. Since all panels must align with the stream-wise direction in DLM, constructing a paneled region there would imply the root side of the wing-tip is a leading edge. This aerodynamic implication would be unrealistic as the physical structure resembles closer to a bluff body due to its thickness rather than a flat plate that DLM is modeling. To compensate for this reduction in total paneled area, a scaling factor was applied to the remaining wing-tip panels such that the total loads would be similar. The scaling was applied proportionally based on area ratio of the missing triangular region and facilitated by changing the lift-curve correction factor (WKK in

NASTRAN) for each applicable panel. It is important to note that DLM can only compute loads normal to the surface of each panel in addition to an associated pitching moment, due to the limitation of the potential flow theory it is based upon. Therefore, no drag can be computed with accuracy regardless of panel configuration. The aeroelastic FEM for the SWP30 configuration has been set up using the same method as well.

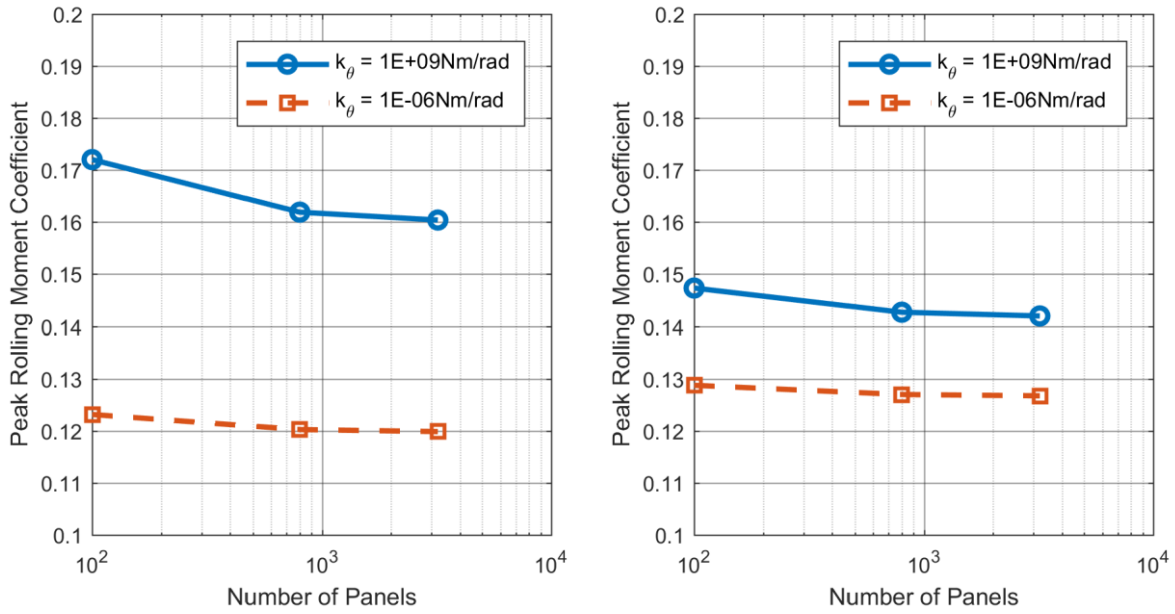

(a) SWP10. (b) SWP30.

Fig. 12 Mesh convergence study on the number of aerodynamic panels.

IV. Results

A. Steady-state

Steady-state measurements were carried out according to the test matrix provided in Table 3. At every test point, the wing-tip settled to a steady fold angle once the flow had stabilized, demonstrating aero-static stability. Steady-state predictions were also calculated using the aeroelastic FEMs in the same condition.

1. Wind tunnel test results

As shown in Fig. 13(a) and (c), both sweep angle configurations with the stiff-hinge arrangement showed linear lift-curves, as expected of a non-folding wing-tip set-up. With the free-hinge arrangement, the SWP10 configuration showed a mostly linear lift-curve with a small drop-off in lift towards high angle of attack in Fig. 13(b). This reduction in lift was due to the fold angle settling above zero, as shown in Fig. 14(b). In these conditions, as shown in Fig. 15 (a), a positive fold angle causes a negative change in wing-tip angle of attack, thus resulting in a reduction in lift from the wing-tip. This effect is further highlighted by Fig. 16(b), which shows the rolling moment was also reduced at higher lifting conditions.

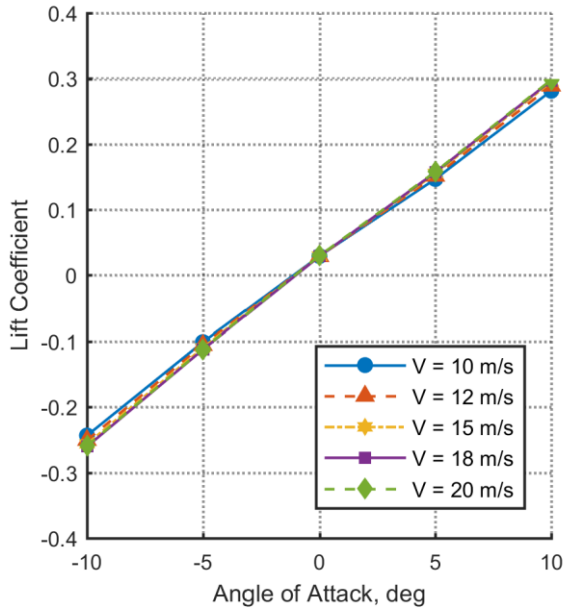

(a) SWP10 with stiff-hinge configuration.

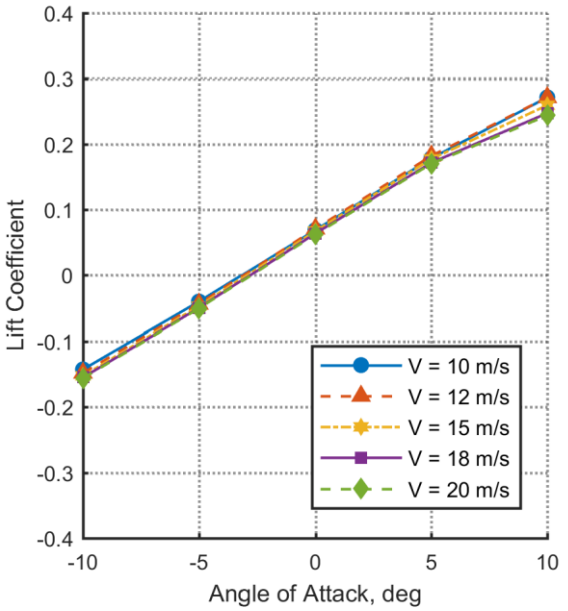

(b) SWP10 with free-hinge configuration.

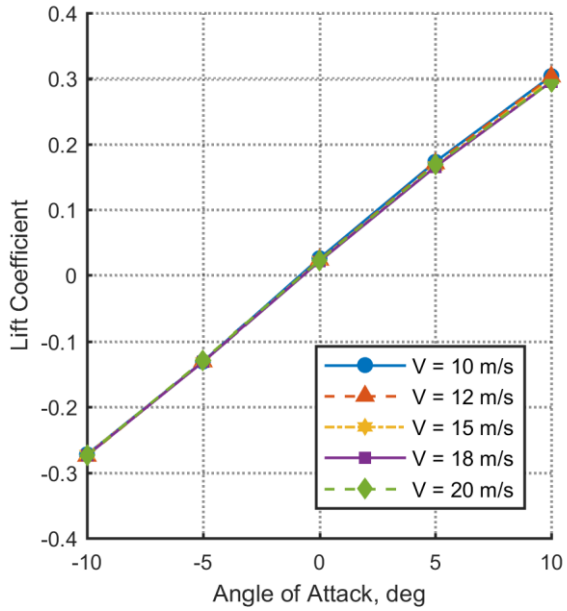

(c) SWP30 with stiff-hinge configuration.

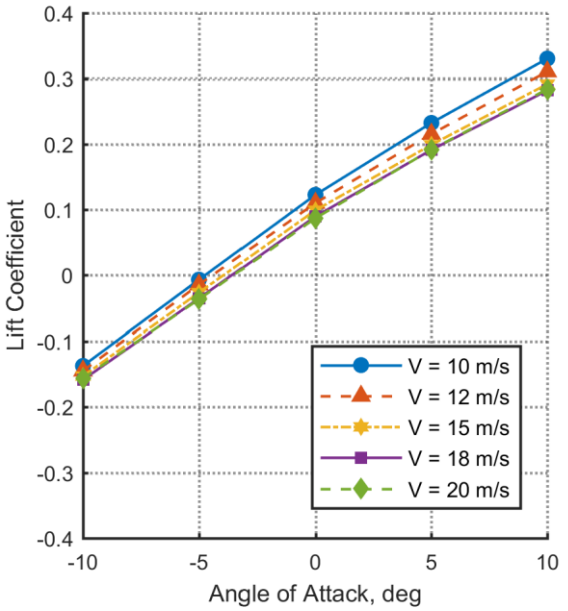

(d) SWP30 with free-hinge configuration.

Fig. 13 Variation of measured lift coefficient with angle of attack.

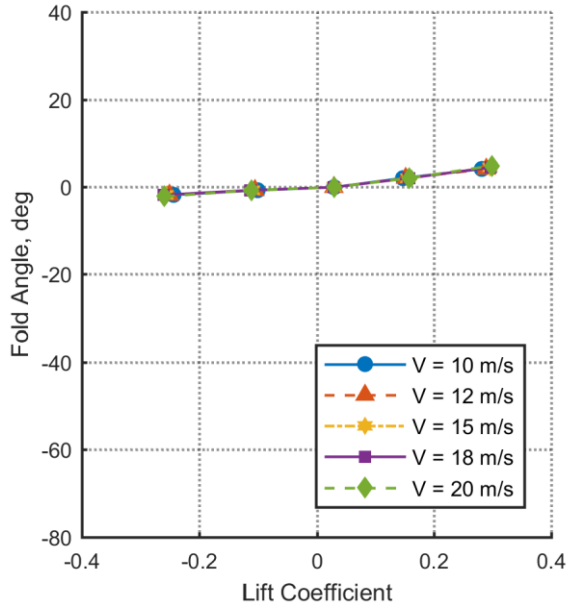

(a) SWP10 with stiff-hinge configuration.

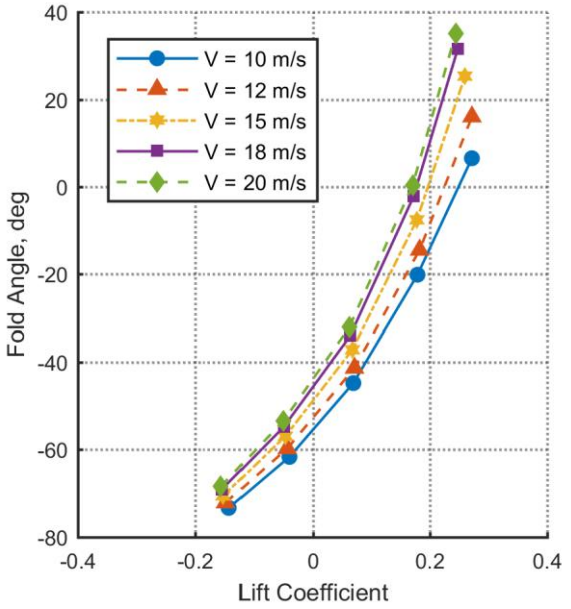

(b) SWP10 with free-hinge configuration.

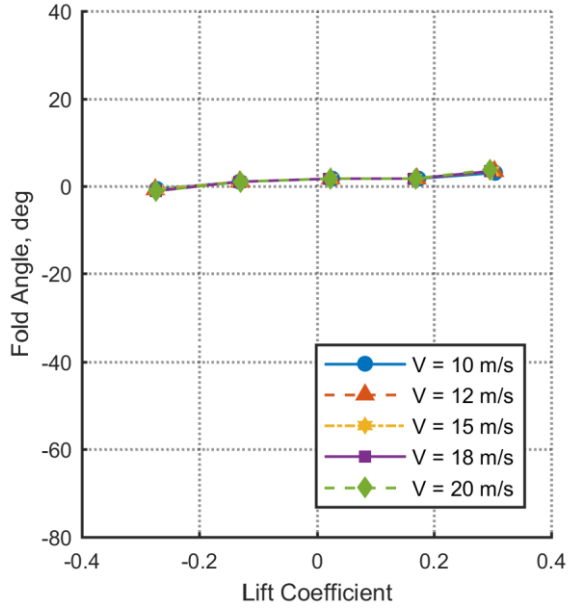

(c) SWP30 with stiff-hinge configuration.

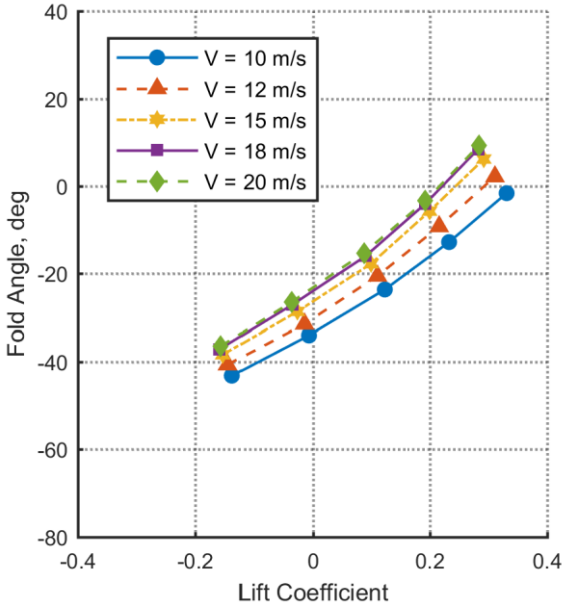

(d) SWP 30 with free-hinge configuration.

Fig. 14 Variation of measured fold angle against measured lift coefficient.

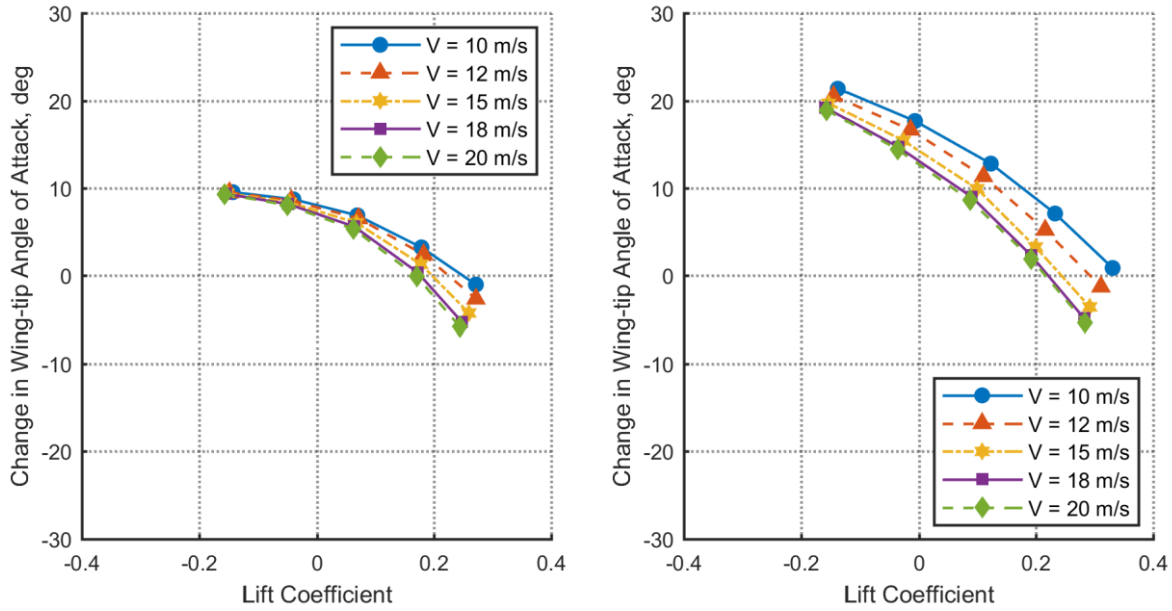

(a) SWP10 with free-hinge configuration. (b) SWP30 with free-hinge configuration.

Fig. 15 Variation of the change in wing-tip angle of attack against measured lift coefficient.

For the SWP30 configuration with the free-hinge arrangement, as shown in Fig. 13(d), the slight reduction in lift-curve slope can be explained in similar manner through comparing the aero-static fold angle provided in Fig. 14(d). As shown in Fig. 15 (b), the change in wing-tip angle of attack was mostly in the positive region in these cases, therefore the wing-tip was in fact producing higher lift than at fold angle of zero degrees. This behavior also explains the more significant lift offset at zero angle of attack than the stiff-hinge arrangement for this symmetric airfoil-based wing. For the rolling moments, as shown in Fig. 16(d), increasing wind tunnel speed shifted the curve downwards because less lift was generated at the wing-tip as the fold angle became more positive.

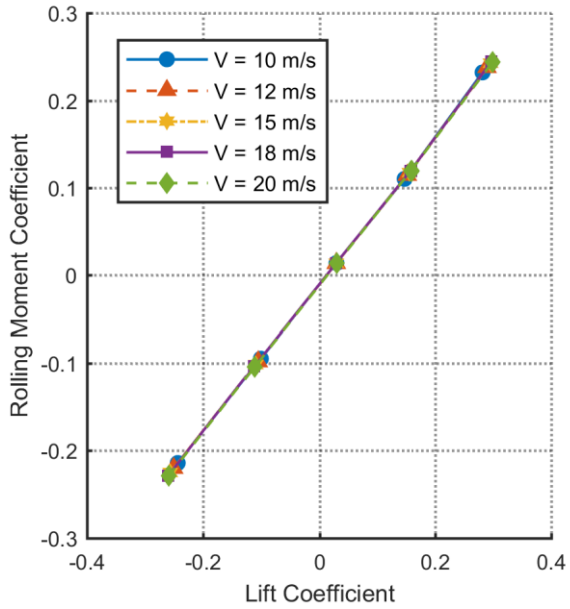

(a) SWP10 with stiff-hinge configuration.

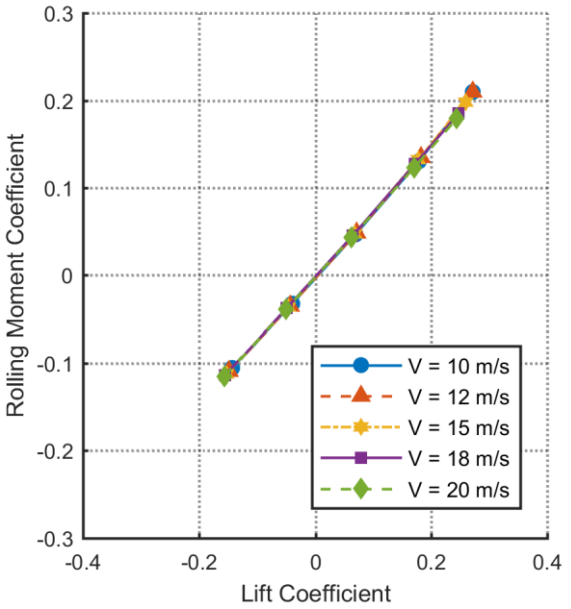

(b) SWP10 with free-hinge configuration.

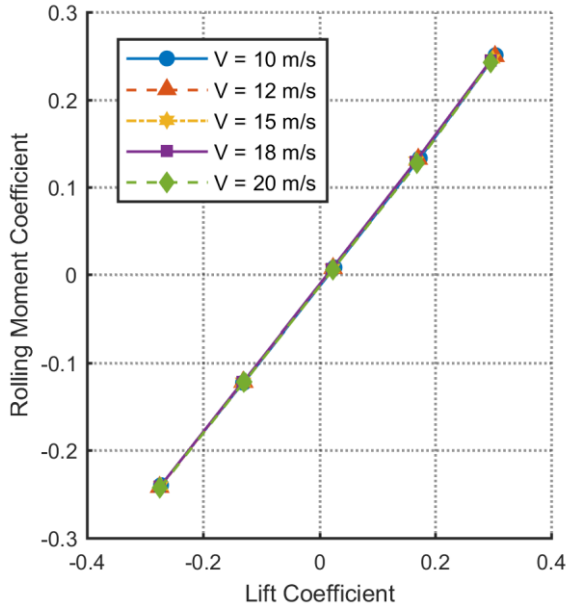

(c) SWP30 with stiff-hinge configuration.

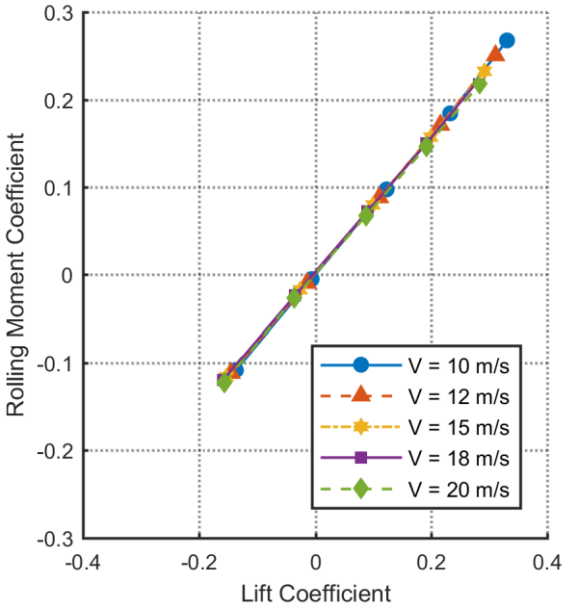

(d) SWP30 with free-hinge configuration.

Fig. 16 Variation of measured rolling moment coefficient against measured lift coefficient.

2. Numerical results

Each FEM was analyzed using SOL144 flexible trim analysis in NASTRAN. Since the weight of the wing-tip produces a moment due to the distance of its center of mass from the hinge line, this moment must be accounted for in the simulation to produce the correct aero-static position in the final solution. However, when the analysis is conducted this way, the loads measured at the boundary constraint are due to both the aerodynamics and the

inertial contribution, therefore an additional step was taken to obtain the net aerodynamic loads. The additional step involved running a separate SOL101 static analysis to simulate the 'wind-off' condition. The results from this static analysis formed the loads measurement datum for eliminating the inertial contribution from the raw flexible trim data.

Fig. 17(a) and (c) respectively show the variation of lift coefficient against angle of attack for the SWP10 and the SWP30 configuration at the highest hinge spring stiffness of k_θ=1E9Nm/rad. In all test cases, the lift curve remained linear and invariant of test velocity. The same is observed in the rolling moment behavior shown in Fig. 18(a) and (c), indicating the span-wise lift distribution did not vary significantly. Although the torsion springs were both set to a very high stiffness, there was still a small degree of flexibility in the remaining structure, giving rise to a small folding deflection of the wing-tip in each case, as illustrated in Fig. 19(a) and (c). The fold angle change for the SWP10 configuration was marginally larger, since the wing-tip is larger in size and weight in this configuration, resulting in a larger moment at the hinge. Overall, the behavior observed is similar to a non-folding wing, showing validity in using this stiffness case as a baseline reference.

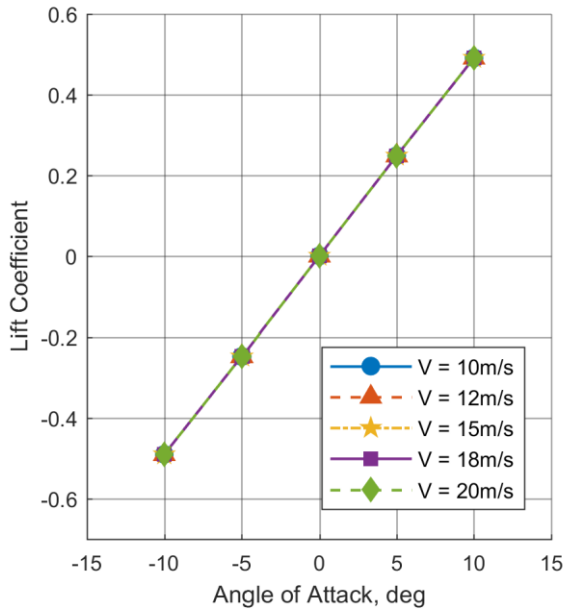

(a) SWP10 with k_θ=1E9Nm/rad.

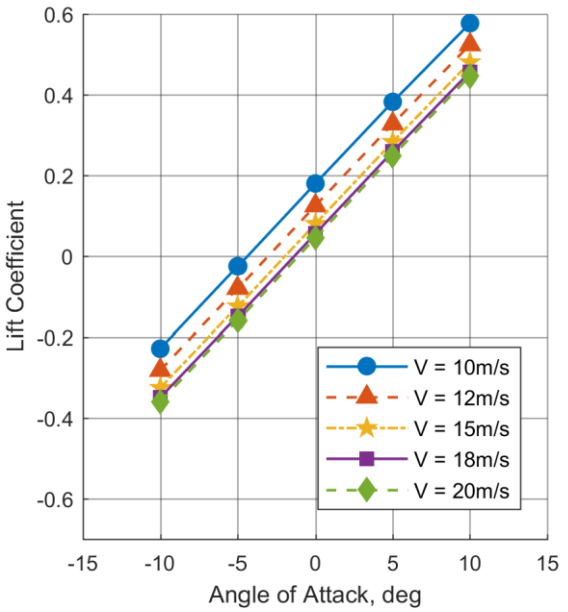

(b) SWP10 with k_θ=1E-6Nm/rad.

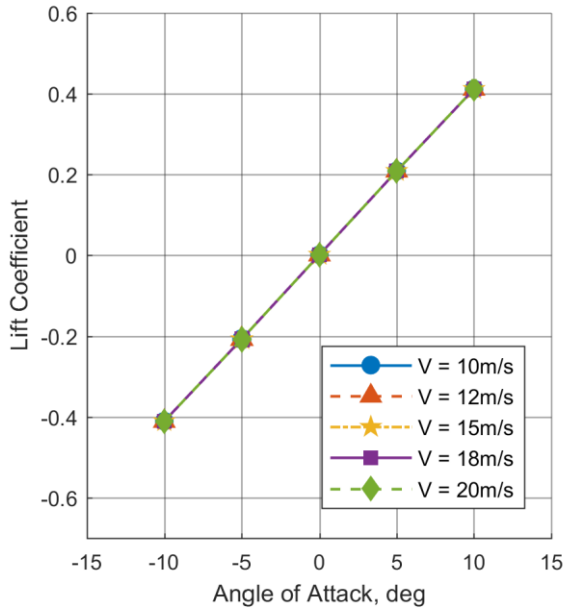

(c) SWP30 with k_θ=1E9Nm/rad.

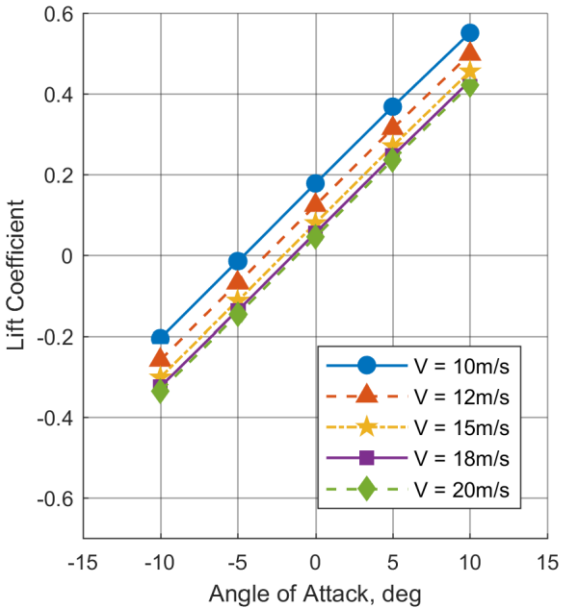

(d) SWP30 with k_θ=1E-6Nm/rad.

Fig. 17 Variation of lift coefficient against angle of attack.

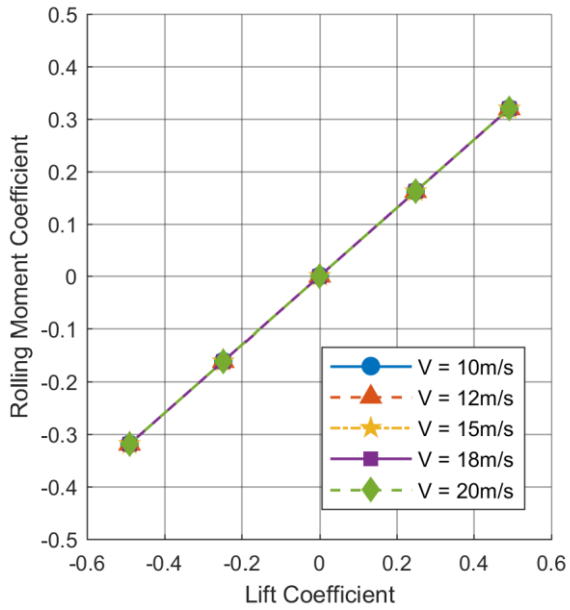

(a) SWP10 with k_θ=1E9Nm/rad.

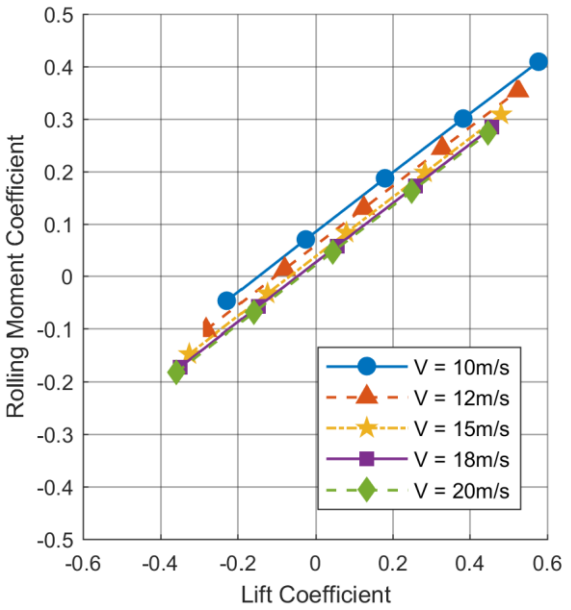

(b) SWP10 with k_θ=1E-6Nm/rad.

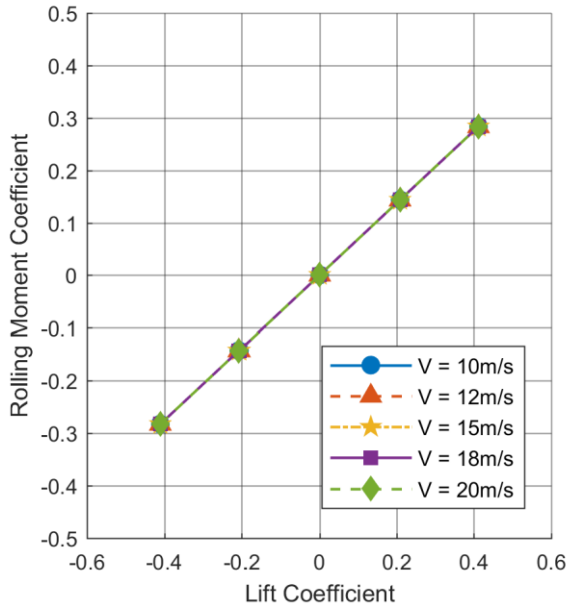

(c) SWP30 with k_θ=1E9Nm/rad.

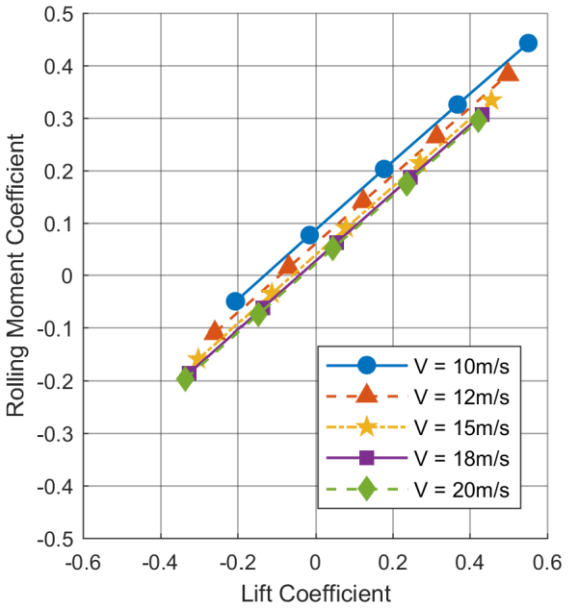

(d) SWP30 with k_θ=1E-6Nm/rad.

Fig. 18 Variation of rolling moment coefficient against lift coefficient.

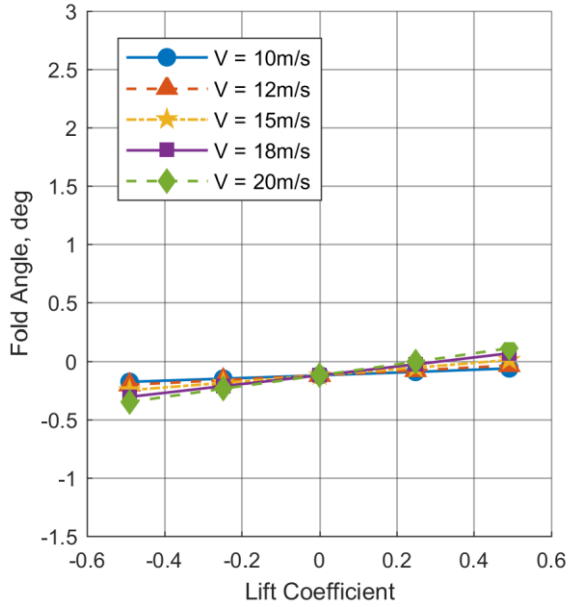

(a) SWP10 with k_θ=1E9Nm/rad.

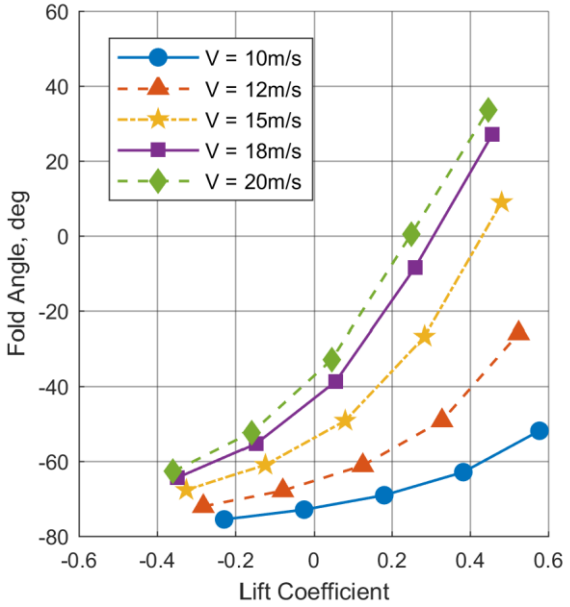

(b) SWP10 with k_θ=1E-6Nm/rad.

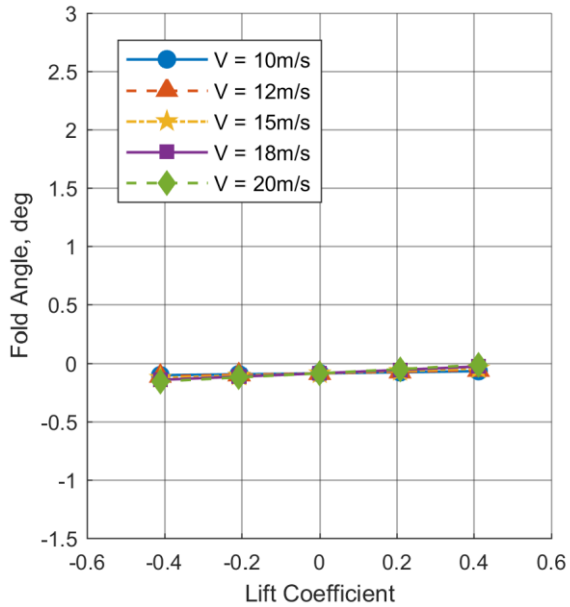

(c) SWP30 with k_θ=1E9Nm/rad.

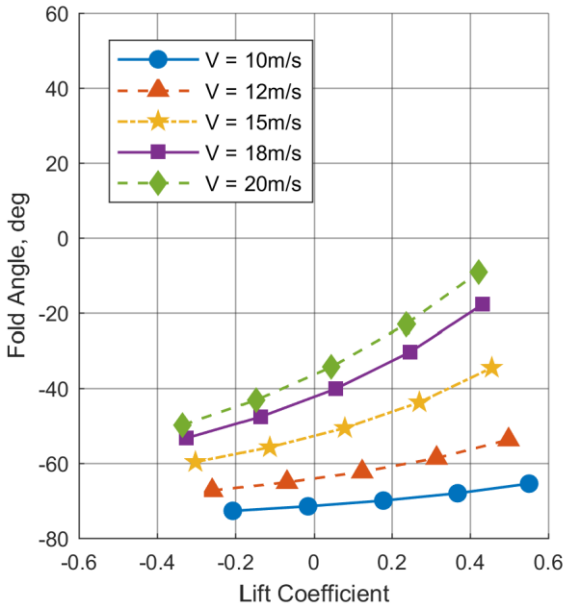

(d) SWP30 with k_θ=1E-6Nm/rad.

Fig. 19 Variation of fold angle against lift coefficient.

For the lowest hinge stiffness configuration of k_θ=1E-6Nm/rad, shown in Fig. 17(b) and (d) for the SWP10 and SWP30 configuration respectively, the lift curves remain linear at each test velocity, but offset to each other. These offsets can be explained by first considering the fold angle of each wing-tip in these conditions, which are shown in Fig. 19(b) and (d). Although there is a relatively large variation in fold angle at different test velocities and lifting conditions, the fold angle was generally more positive as velocity or angle of attack was increased. This behavior can be explained by recognizing the fold angle in steady aerodynamic conditions is governed by

the balance between the hinge moment due to the weight of the wing-tip and the lift generated over the wing-tip itself. At higher velocities, the balance point shifts to a more positive fold angle at positive angle of attack because lift scales with velocity. However, the hinge geometry causes the angle of attack of the wing-tip to decrease at positive fold angle, reducing the local lift generated at the wing-tip itself. Therefore, the overall generated lift is lower than the non-folding configuration when the fold angle is above zero, which explains the lift reduction at higher velocities as seen in Fig. 17(b) and (d). This reduction in lift at the wing-tip due to positive fold angle also caused a negative change in rolling moment due to its distance away from the wing-root, as shown in Fig. 18(b) and (d).

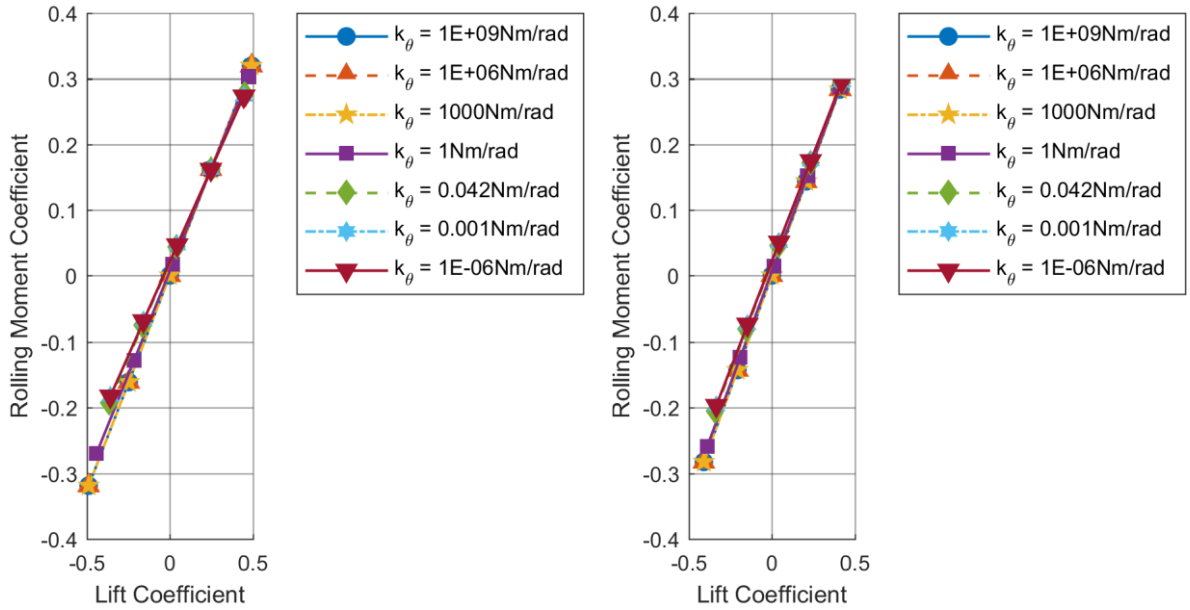

(a) SWP10 (b) SWP30

Fig. 20 Variation of rolling moment coefficient against lift coefficient at 20m/s.

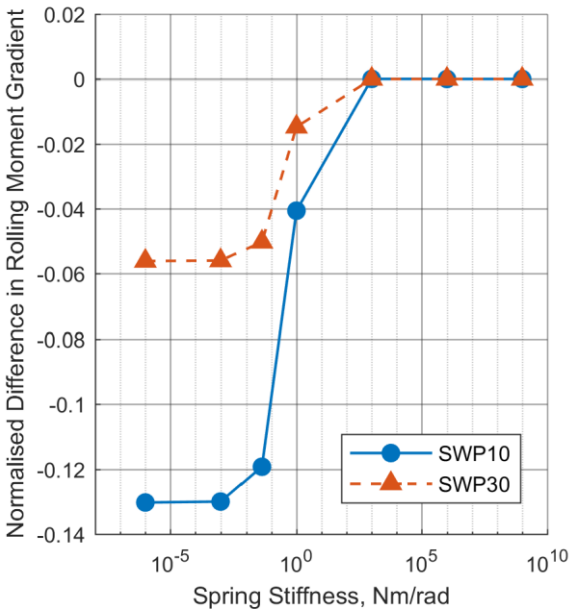

Fig. 21 Normalized difference in rolling moment gradient with respect to lift for various FEMs of different hinge stiffness at 20m/s.

Fig. 20 gives further insight into the influence of hinge stiffness by showing the gradient of the rolling moment curve becoming shallower with decreasing hinge stiffness. The normalized difference in gradient shown in Fig. 21 is based on the gradient of the rolling moment curve from the stiffest hinge configuration of each respective FEM, such that the influence of sweep angle can be minimized when comparing across both sweep/hinge angle configurations. For hinge spring stiffness below k_θ=1E3Nm/rad, the reduction in gradient observed is due to lower stiffness providing less resistive hinge moment, allowing the wing-tip to settle at a larger positive fold angle, leading to less positive lift being generated at the wing-tip. However, this effect is also reversed at negative lifting conditions, giving rise to the lower gradient in the rolling moment curve when compared with the non-folding configuration. This change in gradient appears to be the most sensitive around hinge spring stiffness of k_θ=1Nm/rad, which is further highlighted by the variation observed in the fold angle as illustrated in Fig. 22, where the gradient of the curve changes significantly. As mentioned previously, the aero-static fold angle is dependent on the balance of moments around the folding hinge, therefore sensitivity of these gradient changes is highly likely to be linked to the weight of the wing-tip. Despite this weight-stiffness dependency, the gradient plateaus at low hinge spring stiffness, meaning a wide range of low stiffness configurations could still reduce the bending moment at the wing-root. Since a steady aerodynamic condition for most aircraft can be considered as the cruise condition, this finding suggests the level of wing-root bending moment at cruise could be reduced with

a folding wing-tip of low hinge stiffness. A reduction in the wing-root bending at cruise could benefit fatigue life of the wing and its surrounding structures as well as a potentially lower peak load during gust encounters.

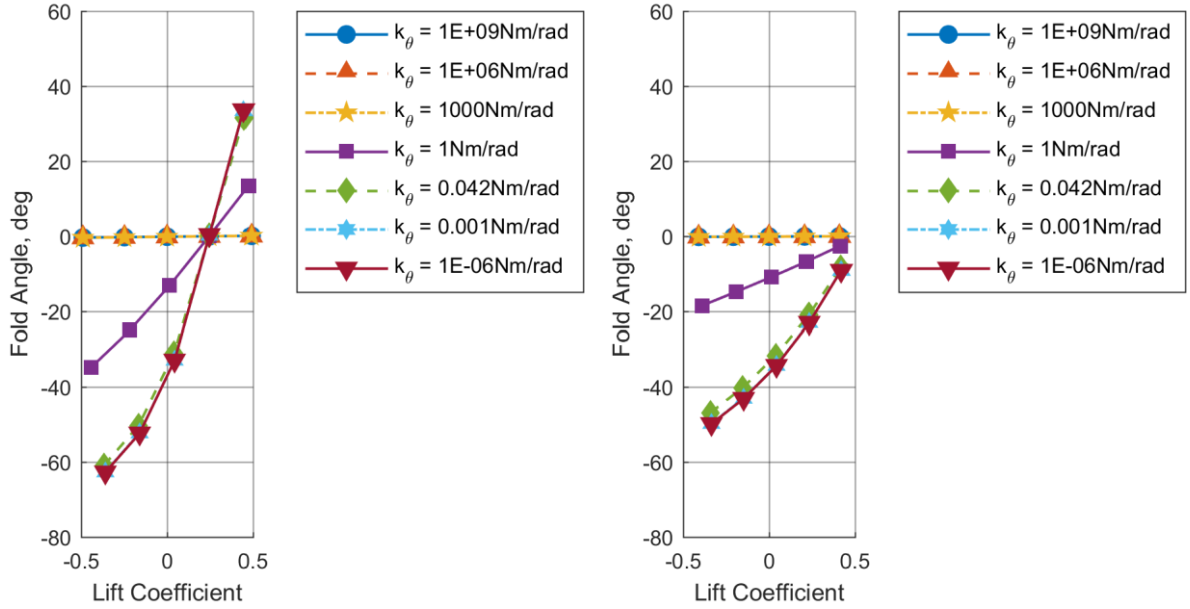

(a) SWP10 (b) SWP30

Fig. 22 Variation of fold angle against lift coefficient at 20m/s.

3. Comparison between numerical and wind tunnel test results

Fig. 23 shows a comparison between the wind tunnel test and FEM results for the SWP10 and the SWP30 configuration respectively. The stiff-hinge arrangement corresponds to the highest equivalent torsional hinge spring stiffness of k_θ=1E9Nm/rad in the FEM, while the free-hinge arrangement is matched with the lowest equivalent torsional hinge spring stiffness of k_θ=1E-6Nm/rad. The low stiffness case is the best approximation to the free-hinge arrangement because NASTRAN cannot produce reliable results when a mechanism is present in the FEM (i.e. k_θ=0Nm/rad).

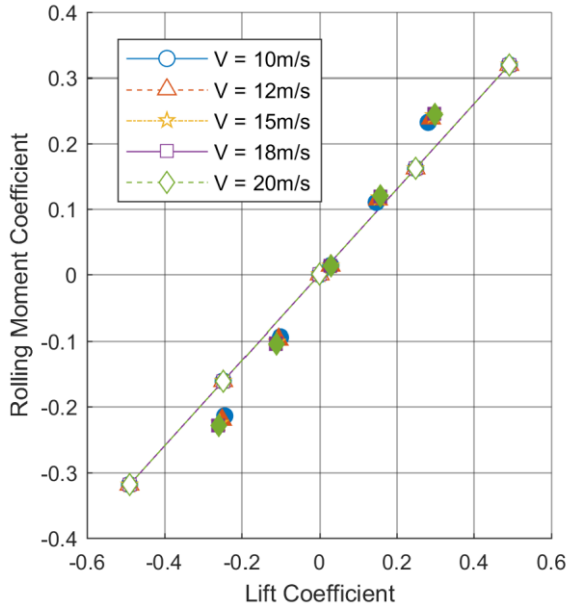

(a) SWP10 with k_θ=1E9Nm/rad against wind tunnel stiff-hinge results.

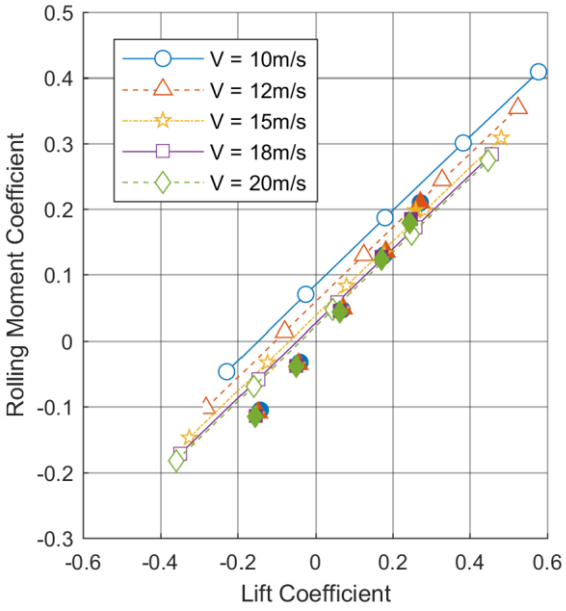

(b) SWP10 with k_θ=1E-6Nm/rad against wind tunnel free-hinge results.

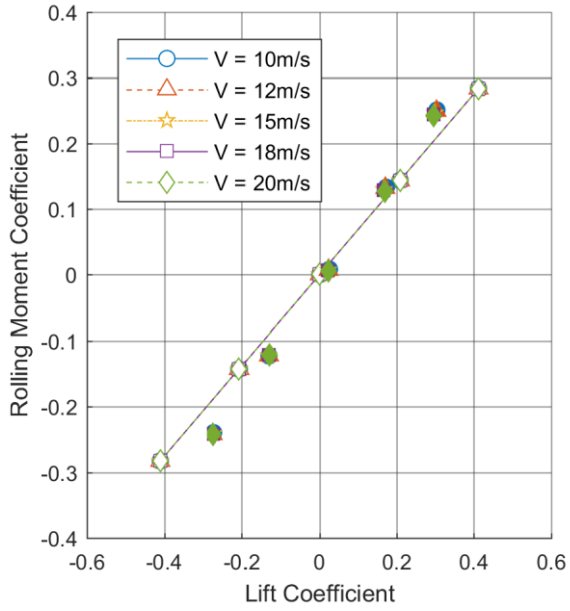

(c) SWP30 with k_θ=1E9Nm/rad against wind tunnel stiff-hinge results.

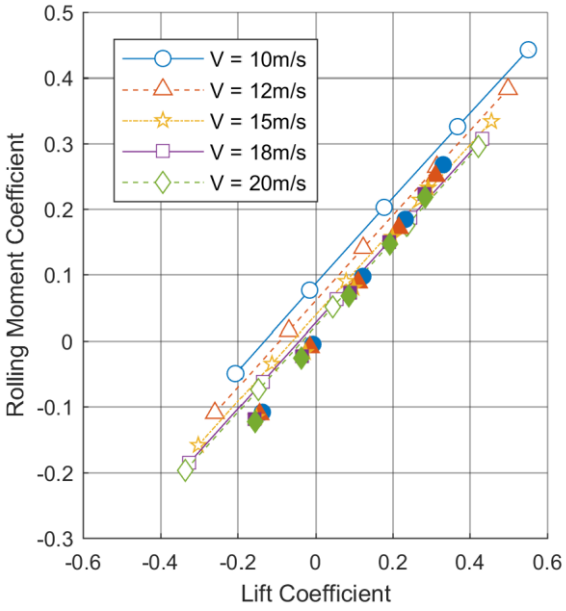

(d) SWP30 with k_θ=1E-6Nm/rad against wind tunnel free-hinge results.

Fig. 23 Variation of rolling moment coefficient against lift coefficient. Computational results and wind tunnel measurements are shown as hollow and filled markers respectively.

Numerical results from both the SWP10 and the SWP30 configuration FEMs show similar trends with the wind tunnel test data for both hinge arrangements, confirming the necessity of the aerodynamic panel modifications within each FEM. However, the wind tunnel results generally show a higher rolling moment

coefficient for a given lift coefficient. This difference is due to the characteristic of the wind tunnel set-up in which the wing-root region was at the boundary of the wind tunnel jet, as shown in Fig. 7(c). Due to the circular nature of cross-section of the wind tunnel jet, more of the inboard region of the wind tunnel model protrude outside of the jet as the angle of attack increases, reducing the lift generated. This arrangement was based on a compromise between flow quality, loads, sensor sensitivity and emphasizing on ensuring the wing-tip remains inside the wind tunnel jet at all fold angles, as shown in Fig. 7(d). Therefore, the wind tunnel results remain valid despite the total lift appearing lower in magnitude.

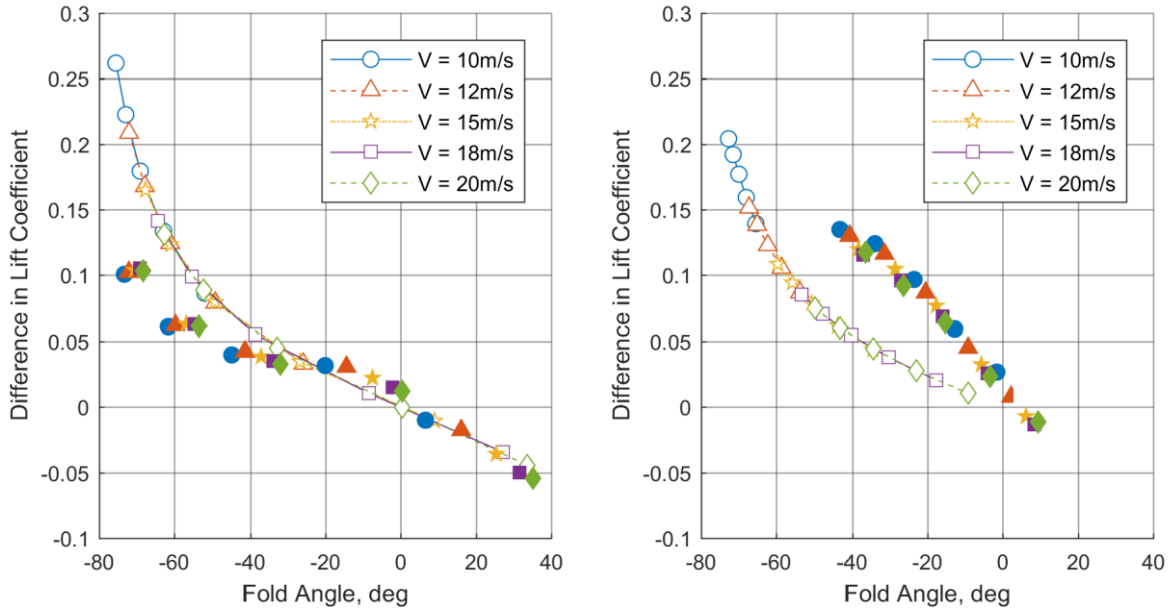

(a) SWP10. (b) SWP30.

Fig. 24 Difference in lift coefficient between the free-hinge and the stiff-hinge case against fold angle. Computational results and wind tunnel measurements are shown as hollow and filled markers respectively.

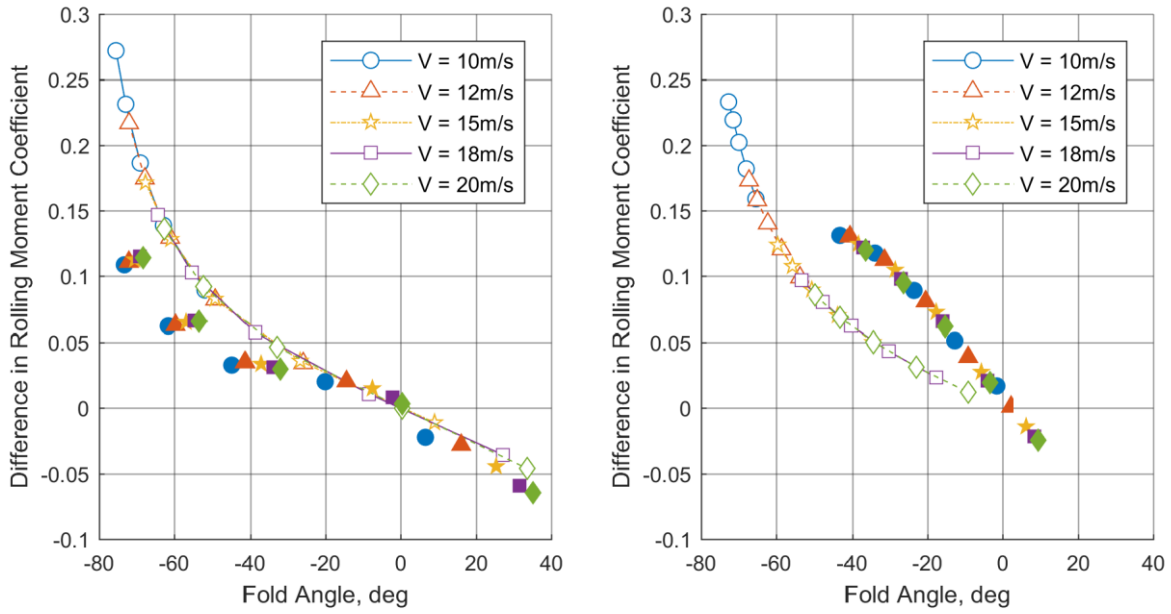

(a) SWP10. (b) SWP30.

Fig. 25 Difference in rolling moment coefficient between the free-hinge and the stiff-hinge case against fold angle. Computational results and wind tunnel measurements are shown as hollow and filled markers respectively.

Using the stiff-hinge results as the datum, the differences in lift and rolling moment against the aero-static fold angle from the free-hinge cases are shown in Fig. 24 and Fig. 25 respectively. The computational results show good agreement for fold angle around zero. However, there is strong evidence that the coupled DLM used in the numerical analysis could not fully capture the coupling between folding and angle of attack change of the wing-tip, because the numerical results of the SWP30 configuration show a more gradual increase in loads with decreasing fold angle compared to the wind tunnel measurements. This discrepancy is more apparent in the SWP30 configuration because the hinge angle is higher, and thus this coupled effect is stronger. The DLM also lacked the ability to replicate the aerodynamic stall of the wing-tip at low fold angles, where the true angle of attack of the wing-tip was near stall, as shown by the reduction in loads below fold angle of -30.0 degrees for the SWP30 configuration. Therefore, constructing an aeroelastic FEM to fully simulate the folding wing-tip concept will require substantial tuning and corrections applied to the DLM. Despite this, the simple DLM correction implemented in this work has provided good prediction in the aero-static behavior of the folding wing-tip concept for cases where the eventual fold angle is near zero.

B. Gust excitation

1. Wind tunnel test results

The SWP10 and the SWP30 configuration were tested according to the test matrix shown in Table 4.At each test point, the wind tunnel model was subjected to a single upward gust, generated through deflecting the gust vane to 10.0 degrees and back. A typical response of the wind tunnel model from such gust excitation is shown in Fig. 26.

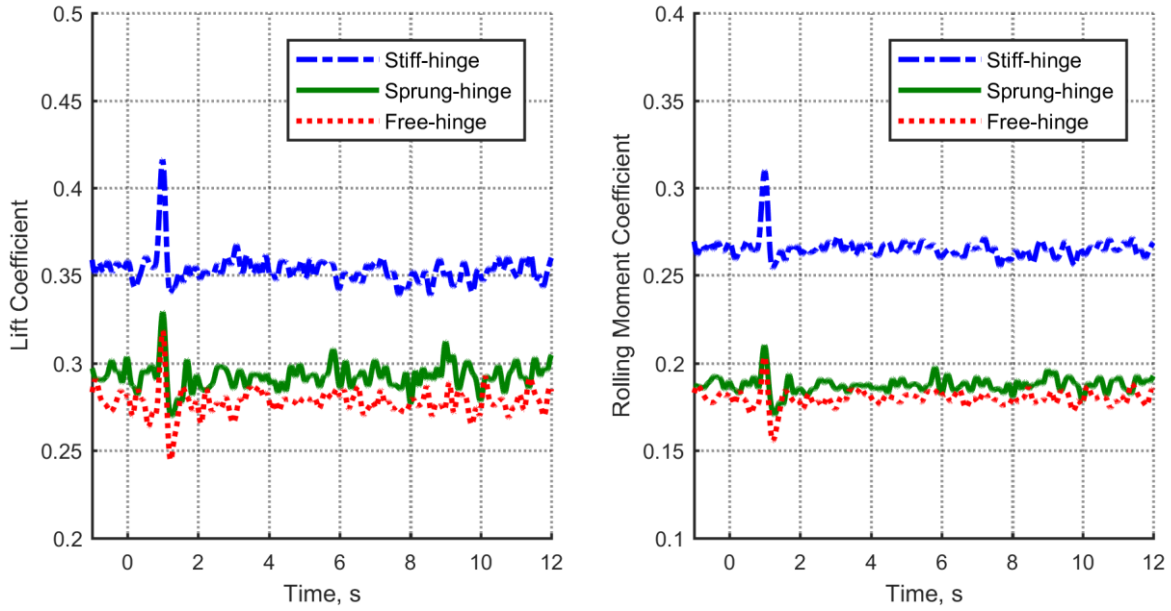

(a) Lift coefficient. (b) Rolling moment coefficient.

Fig. 26 Gust response of the SWP10 configuration at 10 degrees angle of attack and wind speed of 20m/s.

In Fig. 27 and Fig. 28, the upper and lower bound of the dynamic load envelope from the gust excitations are shown. The upper bounds refer to the difference between the maximum in each measurement from the steady state mean and similarly for the lower bounds. In Fig. 27(c) and (f), both the upper and lower bound of the fold angle response for the stiff-hinge arrangement are small, demonstrating the suitability of using the stiff-hinge data as the non-folding wing-tip baseline for the SWP10 configuration. Similarly, the stiff-hinge arrangement for the SWP30 configuration was also set up correctly, basing upon the results shown in Fig. 28(c) and (f).

In Fig. 27(a), both the sprung-hinge and the free-hinge arrangement for the SWP10 configuration are shown to produce lower peak changes in lift across all lifting conditions compared to the stiff-hinge case. The free-hinge arrangement generally had a smaller peak lift loading and the peak rolling moments were also lower as shown in Fig. 27(b). These results suggest the free-hinge arrangement is more effective in solving the main issue in positive vertical gust encounters, where the peak wing-root bending moment increment may become critical for structural integrity. For the lower bound in rolling moment change, as shown in Fig. 27(e), both the sprung-hinge and the

free-hinge arrangement performed similarly to the stiff-hinge arrangement, except at the highest lifting case with lift coefficient of 0.3. In fact, both the sprung-hinge and the free-hinge arrangement had a sudden increase in the magnitude of the rolling moment change from the previously lower lifting conditions. This also coincides with a smaller lower bound in fold angle change as shown in Fig. 27(f). As seen from the steady-state wind tunnel measurements, a more negative fold angle produces higher positive lift at the wing-tip and thus more positive rolling moment is generated as a result. Therefore, the previously lower lifting cases were in fact benefiting from this additional rolling moment for reducing the size of the lower bound. This sudden loss of negative rolling moment alleviation at lift coefficient of 0.3 can be attributed to the highly positive aero-static fold angle of 38 degrees in this condition, as shown in Fig. 14(b). At a fold angle of 38 degrees, the effective angle of attack change in the wing-tip was already at -7.7 degrees, as shown in Fig. 15(a), which meant the wing-tip was less susceptible to folding further upwards during the gust encounter. As a result, there was insufficient downward momentum for the wing-tip to reach a more negative fold angle after the gust had passed.

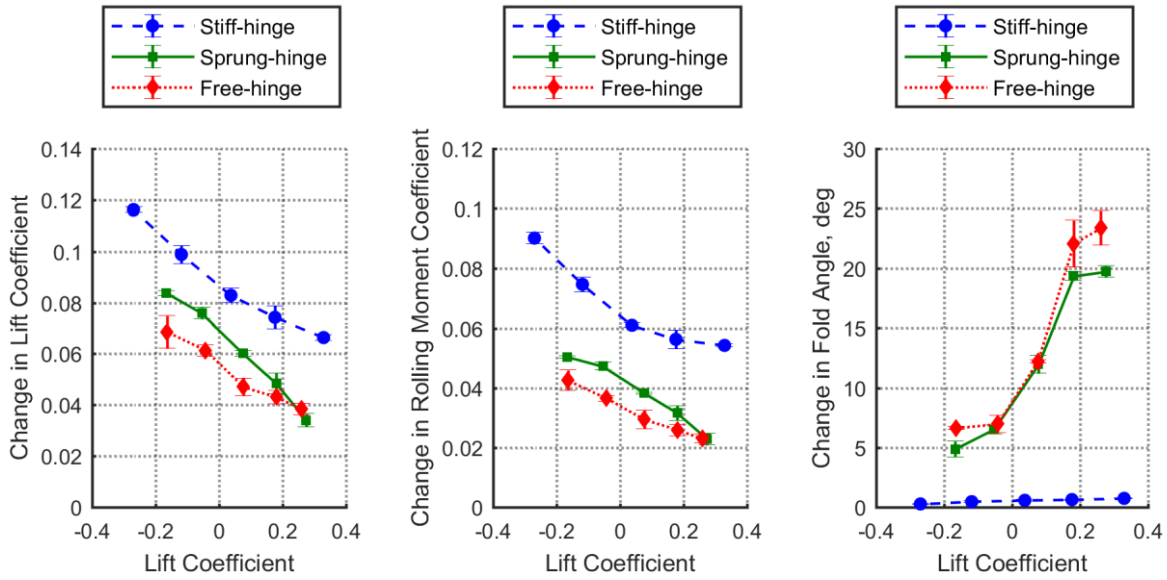

(a) Upper bound of change in lift coefficient.

(b) Upper bound of change in rolling moment coefficient.

(c) Upper bound of change in fold angle.

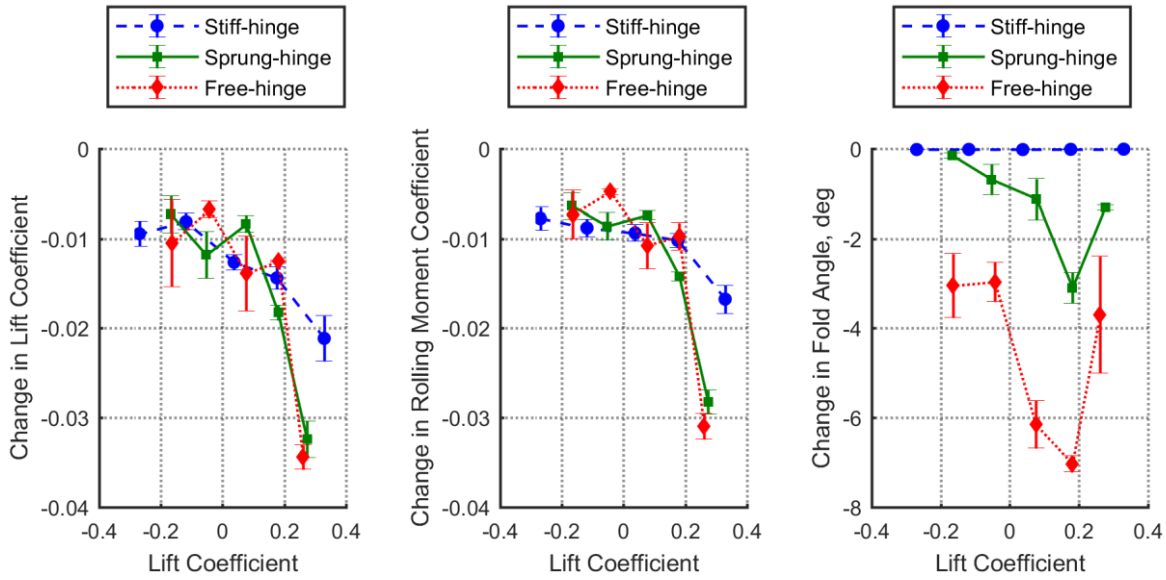

(d) Lower bound of change in lift coefficient.

(e) Lower bound of change in rolling moment coefficient.

(f) Lower bound of change in fold angle.

Fig. 27 Gust response of the SWP10 configuration at wind tunnel speed of 20m/s.

For the SWP30 configuration, the general trend in gust loads alleviation is the same as the SWP10 configuration, which is shown by the lower peak loads in the sprung-hinge and the free-hinge arrangement in Fig. 28(a) and (b). Within these results, the upper bound from the free-hinge arrangement are generally lower, indicating better loads alleviation performance in most of the test conditions. Although the general trend in the lower bound of fold angle change follows the equivalent for the SWP10 configuration, as shown in Fig. 28(f), the sudden increase in lower bound loads at higher lifting conditions was absent. This behavior is consistent with the observation in the SWP10 configuration because the SWP30 configuration had a generally less positive aero-static fold angle. In terms of the fold angle upper bounds, the magnitude observed in the SWP10 configuration was larger than the SWP30 configuration, as shown in Fig. 27(c) and Fig. 28(c). This is a direct effect of an increased hinge angle because a larger, but more negative change in angle of attack is applied to the wing-tip as it folds, meaning more negative lift is generated during the upwards motion of the wing-tip and decelerates the wing-tip more quickly before it can reach a higher fold angle.

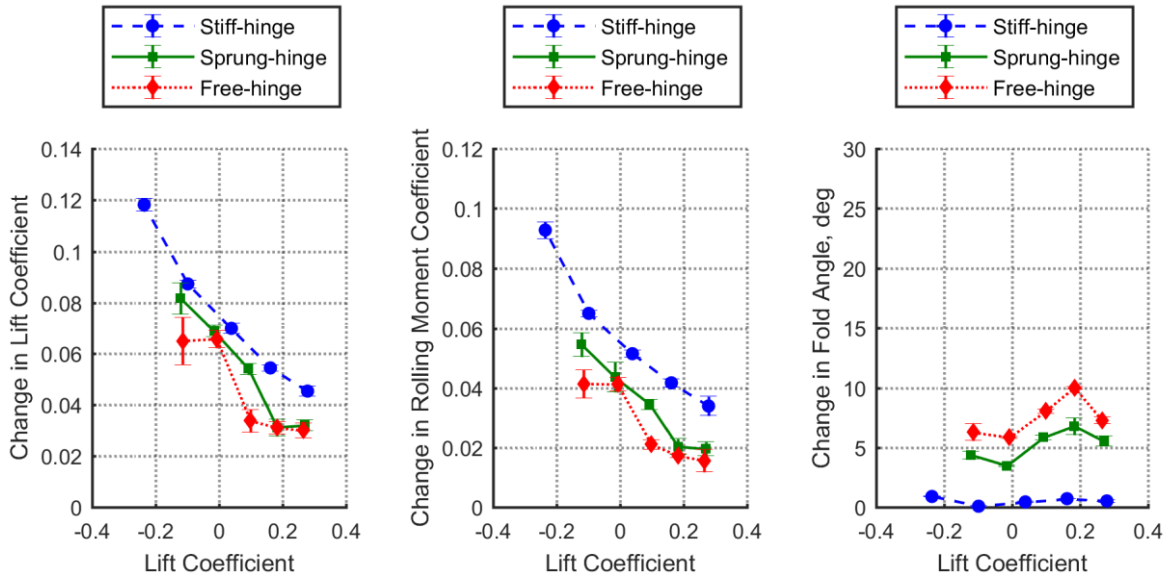

(a) Upper bound of change in lift coefficient.

(b) Upper bound of change in rolling moment coefficient.

(c) Upper bound of change in fold angle.

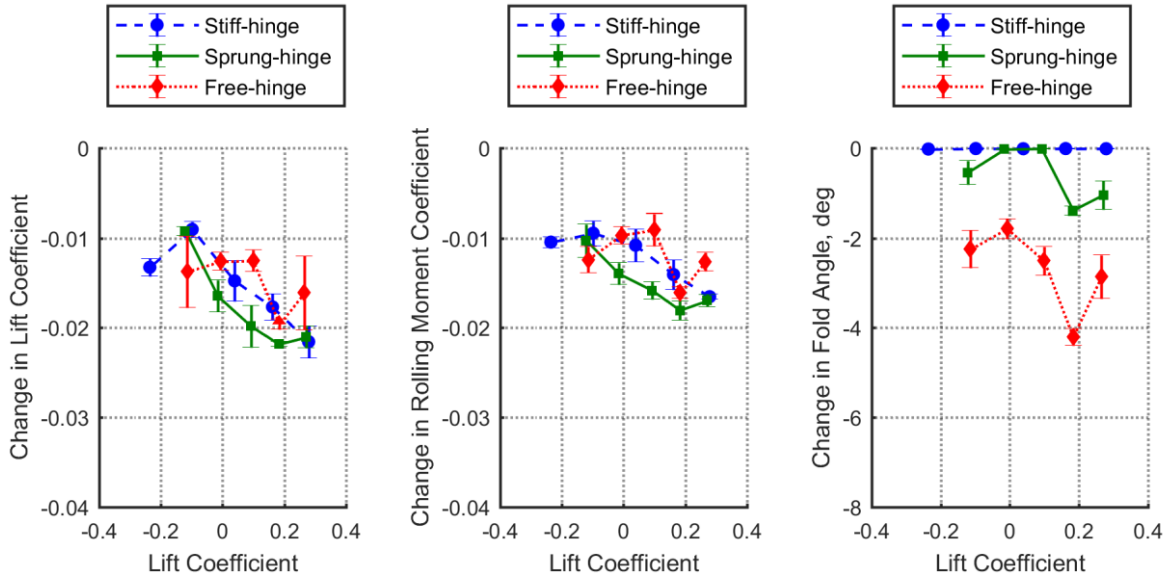

(d) Lower bound of change in lift coefficient.

(e) Lower bound of change in rolling moment coefficient.

(f) Lower bound of change in fold angle.

Fig. 28 Gust response of the SWP30 configuration at wind tunnel speed of 20m/s.

From Fig. 27(b) and Fig. 28(b), the best peak rolling moment reduction in each hinge angle configuration were both 56% with the free-hinge arrangement in operation. For the SWP10 configuration, it occurred at lift coefficient of 0.3 while it was achieved at lift coefficient of 0.1 for the SWP30 configuration. The aero-static fold angle in this case was -20.0 degrees for the SWP30 configuration, as shown in Fig. 14(d), which suggests good gust loads

alleviation performance is still possible with a negative aero-static fold angle, if its magnitude is not excessively large.

2. Numerical simulation

In each simulation, a 1-cosine gust excitation of 8m in length and peak vertical velocity of 1.75m/s was used. This approach was chosen as it is a good approximation to the perturbation generated from the wind tunnel gust vane's motion of 10.0 degrees peak displacement over a period of 0.4s. The gust analysis implemented in NASTRAN is a frequency-domain-based method, therefore the steady state lifting condition of each wind tunnel test could not be fully replicated in the analysis. Instead, each gust simulation assumed the wind tunnel model was in zero-lift condition, with the wing-tip at level-trim orientation.

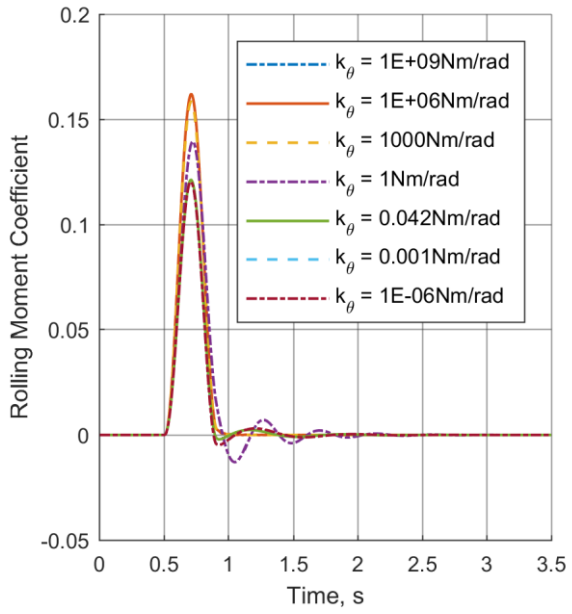

(a) Rolling moment response for SWP10.

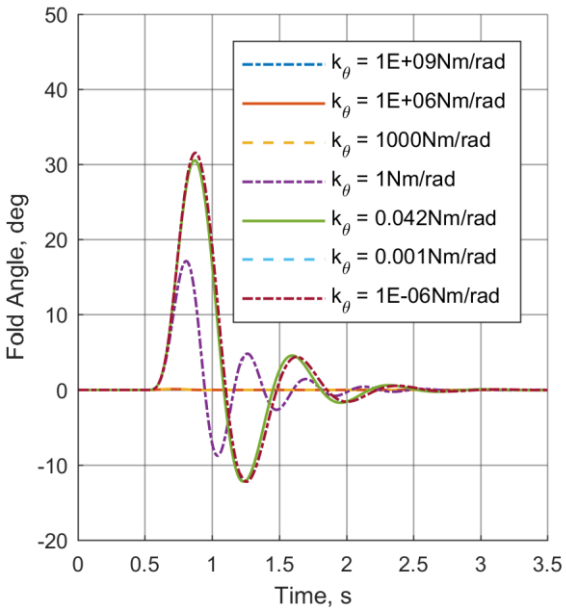

(b) Fold angle response for SWP10.

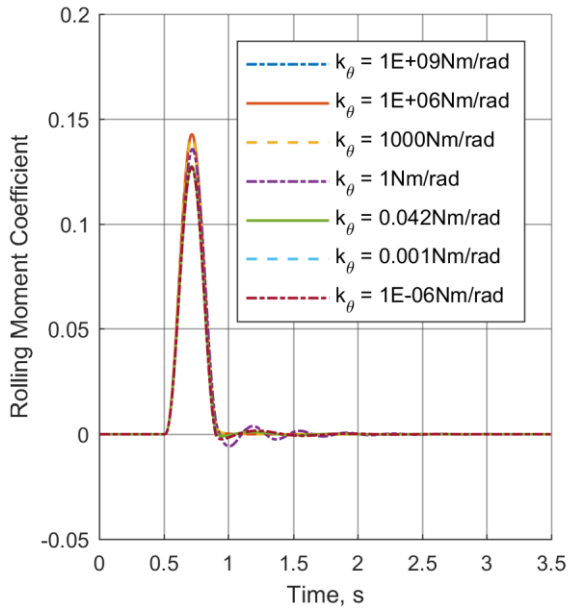

(c) Rolling moment response for SWP30.

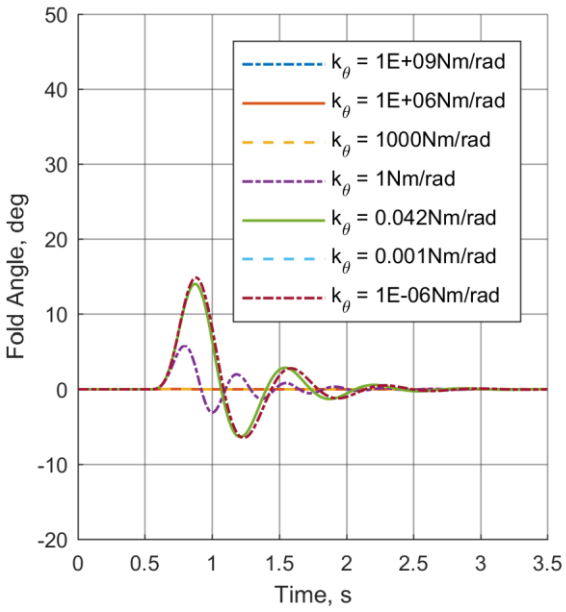

(d) Fold angle response for SWP30.

Fig. 29 Response to gust length of 8m at 20m/s.

In Fig. 29, the peak rolling moment response for both the SWP10 and the SWP30 configurations becomes higher with increased hinge stiffness, while the range of fold angle motion becomes smaller. Such an observation is expected since a higher hinge stiffness tends towards the non-folding configuration.

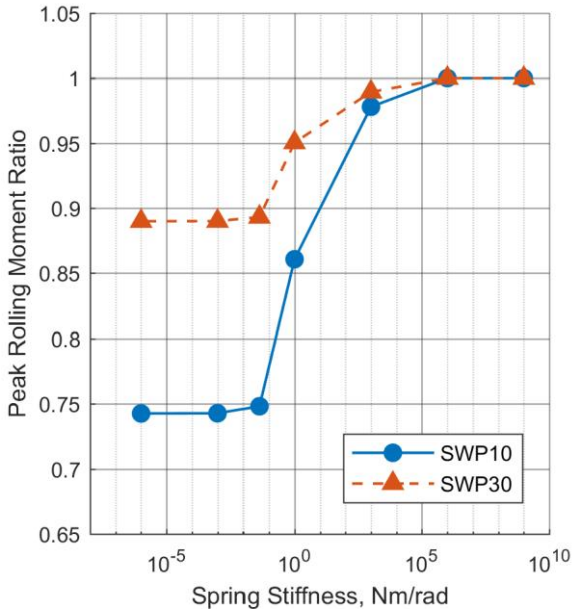

Fig. 30 Comparison of peak rolling moment of various hinge stiffness configurations responding to a gust length of 8m at 20m/s.

In Fig. 30, the ratio of peak rolling moment to the non-folding baseline generally decreases with reduction in hinge spring stiffness. Both the SWP10 and the SWP30 configurations show a plateauing rolling moment

reduction at low spring stiffness. From a design view point, this is favorable as a wider range of spring stiffness could be used without significant loss in performance. As mentioned previously, the limitation of the gust analysis in NASTRAN prevents the analysis to be carried out at the same lifting condition as the wind tunnel experiment, therefore a comparison between these numerical and experimental results could only be conducted in a qualitative manner.

With a hinge spring stiffness of k_θ=0.042Nm/rad, the sprung-hinge configuration has already been shown to perform marginally worse than the free-hinge configuration in Fig. 27(b) and Fig. 28(b). This observation agrees well with the numerical results provided in Fig. 30, as a hinge spring stiffness of k_θ=0.042 Nm/rad corresponds to the region where the gust loads alleviation performance begins to deteriorate. However, the best rolling moment reduction was 26% in the SWP10 configuration and 11% in the SWP30 configuration respectively, which are both significantly short of the 56% reduction recorded from the wind tunnel experiment. This discrepancy was caused by the aforementioned restriction in matching lifting condition, as well as the inability of DLM in accommodating large displacement or rotation of lifting surfaces. In the case of the folding wing-tip, the change in its angle of attack due to large fold angle could not be fully simulated, hence the apparently lower gust loads alleviation performance.

V. Conclusions

For the first time, a folding wing-tip concept with a positive hinge angle has been considered for gust loads alleviation. The first wind tunnel prototype of its kind was constructed and tested in a low-speed wind tunnel to examine its behavior in both steady and dynamic aerodynamic conditions, in conjunction with variation in the stiffness of the folding hinge.

In the steady aerodynamic tests, the folding wing-tip was found to be statically aerodynamically stable with both the stiff-hinge and the free-hinge arrangement, and for both the 10-degree and the 30-degree hinge angle settings, demonstrating inherent aerodynamic stability regardless of hinge stiffness. The free-hinge cases showed shallower overall lift-curves and lower rolling moments with increasing wind tunnel speed. This effect is a direct result of the positive hinge angle inducing a reduction in the angle of attack of the wing-tip and lowering lift generation as wing-tip folds.

The steady measurements have been compared with aeroelastic predictions generated using NASTRAN Finite Element models couple with the Doublet Lattice Method as well. The trends from both sets of measurements were similar, but good agreement was only observed when the fold angle was near zero. Therefore, this computational

approach is only suitable for approximating the aero-static behavior of the folding wing-tip concept if the resultant fold angle is near zero.

The gust excitation tests were conducted using the 10-degree and the 30-degree hinge angle configuration. In both configurations, it was found that the free-hinge arrangement, and the sprung-hinge arrangement of intermediate hinge stiffness, could provide significant reduction in peak rolling moment increment during gust excitations, thus demonstrating gust loads alleviation capability. The free-hinge arrangement appeared to marginally outperform the sprung-hinge arrangement with the best case reaching a 56% reduction in peak rolling moment when compared with the stiff-hinge baseline.

Numerical results generated by the aeroelastic NASTRAN Finite Element models show similar trends to the experimental data in terms of gust loads alleviation performance with respect to changes in hinge spring stiffness for both the 10-degree and the 30-degree hinge angle configuration. However, the predicted load reduction in each case was lower than the achieved reduction from the wind tunnel measurements. This finding suggests the Doublet Lattice Method-based gust analysis implemented in NASTRAN is indeed incompatible with large deflection or rotation of lifting surfaces, which is required for simulating the gust response of the folding wing-tip concept.

VI. Acknowledgments

This work is part of the “Wing Design Methodology Validation” (WINDY) project, which is funded by Innovate UK (Project Reference 113074). The partners in the project are Airbus Group, ARA, Future, Renishaw, University of Bristol and Cranfield University.

The authors would like to thank Andrea Castrichini for his help with the background information.

References

[1] Ajaj, R. M., Beaverstock, C. S., and Friswell, M. I. "Morphing aircraft: The need for a new design philosophy," *Aerospace Science and Technology* Vol. 49, 2016, pp. 154-166.doi: 10.1016/j.ast.2015.11.039

[2] Livne, E., and Weisshaar, T. A. "Aeroelasticity of Nonconventional Airplane Configurations-Past and Future," *Journal of Aircraft* Vol. 40, No. 6, 2003, pp. 1047-1065.doi: 10.2514/2.7217

[3] Silvestro, B., Onur, B., Rafic, M. A., Michael, I. F., and Daniel, J. I. "A Review of Morphing Aircraft," *Journal of Intelligent Material Systems and Structures* Vol. 22, No. 9, 2011, pp. 823-877.doi: 10.1177/1045389X11414084

[4] Friswell, M. "The prospects for morphing aircraft," *IV ECCOMAS Thematic Conference on Smart Structures and Materials*. 2009.

[5] Sofla, A. Y. N., Meguid, S. A., Tan, K. T., and Yeo, W. K. "Shape morphing of aircraft wing: Status and challenges," *Materials & Design* Vol. 31, No. 3, 2010, pp. 1284-1292.doi: 10.1016/j.matdes.2009.09.011

[6] Jian, S., Qinghua, G., Yanju, L., and Jinsong, L. "Morphing aircraft based on smart materials and structures: A state-of-the-art review," *Journal of Intelligent Material Systems and Structures* Vol. 27, No. 17, 2016, pp. 2289-2312.doi: 10.1177/1045389X16629569

[7] Cooper, J. E., Chekkal, I., Cheung, R. C. M., Wales, C., Allen, N. J., Lawson, S., Peace, A. J., Cook, R., Standen, P., Hancock, S. D., and Carossa, G. M. "Design of a Morphing Wingtip," *Journal of Aircraft* Vol. 52, No. 5, 2015, pp. 1394-1403.doi: 10.2514/1.C032861

[8] Smith, M. H., Renzelmann, M. E., and Marx, A. D. "Folding wing-tip system." The Boeing Company, 1995.

[9] Miller, S., Cooper, J., and Vio, G. "Development of an Adaptive Wing Tip Device," *50th AIAA/ASME/ASCE/AHS/ASC Structures, Structural Dynamics, and Materials Conference*. American Institute of Aeronautics and Astronautics, 2009.

[10] Cooper, J., Miller, S., Sensburg, O., and Vio, G. "Optimization of a Scaled Sensorcraft Model with Passive Gust Alleviation," *12th AIAA/ISSMO Multidisciplinary Analysis and Optimization Conference*. American Institute of Aeronautics and Astronautics, 2008.

[11] Guo, S., Li, D., and Sensburg, O. "Optimal design of a passive gust alleviation device for a flying wing aircraft," *12th AIAA Aviation Technology, Integration, and Operations (ATIO) Conference and 14th AIAA/ISSMO Multidisciplinary Analysis and Optimization Conference*. American Institute of Aeronautics and Astronautics, 2012.

[12] Guo, S., Los Monteros, D., Espinosa, J., and Liu, Y. "Gust Alleviation of a Large Aircraft with a Passive Twist Wingtip," *Aerospace* Vol. 2, No. 2, 2015, pp. 135-154.doi: 10.3390/aerospace2020135

[13] Sergio, R., Michele, C., and Giulio, R. "Multi-fidelity design of aeroelastic wing tip devices," *Proceedings of the Institution of Mechanical Engineers, Part G: Journal of Aerospace Engineering* Vol. 227, No. 10, 2012, pp. 1596-1607.doi: 10.1177/0954410012459603

[14] Castrichini, A., Siddaramaiah, V. H., Calderon, D. E., Cooper, J. E., Wilson, T., and Lemmens, Y. "Preliminary investigation of use of flexible folding wing tips for static and dynamic load alleviation," *The Aeronautical Journal* Vol. 121, No. 1235, 2017, pp. 73-94.doi: 10.1017/aer.2016.108

[15] Rodrigues, O. "Des lois géométriques qui régissent les déplacements d'un système solide dans l'espace, et de la variation des coordonnées provenant de ces déplacements considérés indépendamment des causes qui peuvent les produire.," *Journal de Mathématiques Pures et Appliquées* Vol. 5, 1840, pp. 380-440.

[16] Wilson, T., Castrichini, A., Azabal, A., Cooper, J. E., Ajaj, R., and Herring, M. "Aeroelastic Behaviour of Hinged Wing Tips," *International Forum on Aeroelasticity and Structural Dynamics*. Como, Italy, 2017.

[17] Gatto, A., Mattioni, F., and Friswell, M. I. "Experimental Investigation of Bistable Winglets to Enhance Aircraft Wing Lift Takeoff Capability," *Journal of Aircraft* Vol. 46, No. 2, 2009, pp. 647-655.doi: 10.2514/1.39614

[18] Andres, F. A., Onur, B., Michael, I. F., and Peter, H. "Dynamic control for morphing of bi-stable composites," *Journal of Intelligent Material Systems and Structures* Vol. 24, No. 3, 2012, pp. 266-273.doi: 10.1177/1045389X12449918

[19] Castrichini, A., Hodigere Siddaramaiah, V., Calderon, D. E., Cooper, J. E., Wilson, T., and Lemmens, Y. "Nonlinear Folding Wing Tips for Gust Loads Alleviation," *Journal of Aircraft* Vol. 53, No. 5, 2016, pp. 1391-1399.doi: 10.2514/1.C033474

[20] Castrichini, A., Cooper, J. E., Wilson, T., Carrella, A., and Lemmens, Y. "Nonlinear Negative Stiffness Wingtip Spring Device for Gust Loads Alleviation," *Journal of Aircraft* Vol. 54, No. 2, 2016, pp. 627-641.doi: 10.2514/1.C033887

[21] National Instruments, http://www.ni.com/en-gb.html, retrieved 15 June 2017

[22] AMTI, http://www.amti.uk.com/, retrieved 15 June 2017

[23] RLS, http://www.rls.si/, retrieved 15 June 2017

[24] Albano, E., and Rodden, W. P. "A doublet-lattice method for calculating lift distributions on oscillating surfaces in subsonic flows," *AIAA Journal* Vol. 7, No. 2, 1969, pp. 279-285.doi: 10.2514/3.5086

[25] Rodden, W. P., and Johnson, E. H. *MSC/NASTRAN aeroelastic analysis: user's guide; Version 68*: MacNeal-Schwendler Corporation, 1994.